

# Comparative anatomy of geophysical flow models and modeling assumptions using uncertainty quantification

Abani K. Patra<sup>1,3</sup>, Andrea Bevilacqua<sup>2</sup>, Ali Akhavan-Safaei<sup>1</sup>, E. Bruce Pitman<sup>4</sup>, Marcus I. Bursik<sup>2</sup>, and David Hyman<sup>2</sup>

<sup>1</sup>*Dept. of Mech. and Aero. Eng., University at Buffalo, Buffalo NY 14260*

<sup>2</sup>*Dept. of Geology, University at Buffalo, Buffalo NY 14260*

<sup>3</sup>*Comp. Data Science and Eng., University at Buffalo, Buffalo NY 14260*

<sup>4</sup>*Dept. of Materials Design and Innovation, University at Buffalo, NY, 14260*

{abani, abevilac, aliakhav, pitman, mib, davidhy}@buffalo.edu

## Contents

<b>1</b>	<b>Introduction to geophysical mass flows modeling</b>	<b>3</b>
<b>2</b>	<b>Overview of the models</b>	<b>4</b>
2.1	Modeling assumptions . . . . .	4
2.2	Governing equations and numerical solver . . . . .	5
2.3	Rheology assumptions . . . . .	6
2.3.1	Mohr-Coulomb . . . . .	6
2.3.2	Pouliquen-Forterre . . . . .	8
2.3.3	Voellmy-Salm . . . . .	9
2.4	Overview of the case studies . . . . .	10
<b>3</b>	<b>Uncertainty quantification process</b>	<b>11</b>
3.1	General formulation . . . . .	11
3.2	Forces terms definition . . . . .	13
3.3	Alignment and consistency of the input ranges . . . . .	14
<b>4</b>	<b>Results of small scale flows on inclined plane and flat runway</b>	<b>18</b>
4.1	Observable outputs . . . . .	18
4.1.1	Flow height . . . . .	19
4.1.2	Flow acceleration . . . . .	20
4.1.3	Flow extents and spatial integrals . . . . .	21
4.2	Statistical analysis of dynamic quantities . . . . .	22
4.2.1	Power terms . . . . .	22
4.2.2	Force dominance factors . . . . .	23
<b>5</b>	<b>Results of large scale flows on the SW slope of Volcán de Colima (MX)</b>	<b>25</b>
5.1	Flow height overview - Mohr-Coulomb model . . . . .	25
5.2	Observable outputs - UQ on six selected locations . . . . .	26
5.2.1	Flow height . . . . .	26
5.2.2	Flow acceleration . . . . .	29

5.2.3	Flow area and spatial integrals . . . . .	30
5.3	Statistical analysis of dynamic quantities . . . . .	31
5.3.1	Power terms . . . . .	31
5.3.2	Force dominance factors . . . . .	32
<b>6</b>	<b>Discussion on the comparative anatomy of geophysical flow models</b>	<b>35</b>
6.1	Characteristic features and their motivations . . . . .	35
6.1.1	Flow height . . . . .	35
6.1.2	Flow acceleration . . . . .	35
6.1.3	Flow extents and spatial integral . . . . .	35
6.1.4	Power and force terms . . . . .	36
6.1.5	Force dominance factors . . . . .	36
<b>7</b>	<b>Conclusions</b>	<b>37</b>
<b>8</b>	<b>Appendix A: Latin Hypercubes and orthogonal arrays</b>	<b>37</b>
<b>9</b>	<b>Appendix B: Force contribution coefficients, and their conditional decomposition</b>	<b>39</b>

## Abstract

Dense large scale granular avalanches are a complex class of flows with physics that has often been poorly captured by models that are computationally tractable. Sparsity of actual flow data (usually only a posteriori deposit information is available), and large uncertainty in the mechanisms of initiation and flow propagation, make the modeling task challenging, and a subject of much continuing interest. Models that appear to represent the physics well in certain flows, may turn out to be poorly behaved in others, due to intrinsic mathematical or numerical issues. Nevertheless, given the large implications on life and property, many models with different modeling assumptions have been proposed.

While inverse problems can shed some light on parameter choices, it is difficult to make firm judgements on the validity or appropriateness of any single or set of modeling assumptions for a particular target flow, or potential flows, that needs to be modeled for predictive use in hazard analysis. We present here an uncertainty quantification based approach to carefully analyze the effect of several modeling assumptions on quantities of interest in simulations based on three established models, i.e Mohr-Coulomb, Pouliquen-Forsterre and Voellmy-Salm. In doing this, we take advantage of the versatile implementation of all the models on the same infrastructure, given by TITAN2D.

Statistical analysis is performed on spatially averaged dynamical quantities, but also focusing on locally sampled points of interest. This enables us to exploit the significant differences that remain hidden in the averaged analysis. The fundamental focus of this paper is the exploration of the dynamics of the simulated flows, enabling a notion of the contribution of different mechanisms or models elements inside the simulation procedure, in a fully quantitative, predictive-use oriented and statistical framework.

# 1 Introduction to geophysical mass flows modeling

Geophysical mass flows include debris and mud flows, landslides, snow and rock avalanches, glacier flows, pyroclastic surges, block and ash flows, and pumice flows, lahars, jökulhaups and many other examples. These flows are sometimes tens of kilometers in length and may travel at speeds as fast as hundreds of meters per second. Their deposits can be as much as tens of meters deep and kilometers long. In other words, there is no single universal description of a “typical” geophysical mass flow. Different types of flows are the results of different types of mechanisms/processes and hence different types of flows will have significantly different physical characteristics.

The rheology complexity of the fluidized material, and the mathematical problem of modeling and computing, make the description of the dynamics of those flows really challenging. In many cases the flows are *shallow*, i.e. the horizontal dimension is significantly larger than the flow depth. This assumption allows to perform depth-integration on the governing 3D Navier-Stokes equations, resulting in the 2D formulation of Shallow Water Equations (SWE), also known as Saint Venant Equations (Batchelor, 2000; Luca et al., 2016). Pioneering work of Savage and Hutter (1989) that was followed by Hutter et al. (1993); Dade and Huppert (1998) developed a depth-averaged model for flow of granular materials. Their model was used to model a flow of granular material down an inclined plane, originally using the Mohr-Coulomb rheology (MC) (see also Jaeger et al. (1989); Fracccarollo and Toro (1995)). Afterwards, large number of studies focused on the modeling of granular flows, including geophysical mass flows, using SWE approach and many of them were carefully reviewed in Pudasaini and Hutter (2007).

Modeling flow of granular material down an inclined plane was explored in detail by several further studies, both theoretically and experimentally (Pouliquen, 1999; Ruyer-Quil and Manneville, 2000; Silbert et al., 2001; Bursik et al., 2005; DaCruz et al., 2005). Granular material slumping (Balmforth and Kerswell, 2005; Lajeunesse et al., 2005), rapid flow down smooth inclines (Greve et al., 1994; Wieland et al., 1999) and shock waves (Gray et al., 2003; Hokanardottir and Hogg, 2005) were modeled and tested. Terrain erosion effects were investigated (Pitman et al., 2003a; Edwards and Gray, 2015), and also material deposition and self-channeling effects (Mangeney-Castelnau et al., 2005, 2007).

In particular, the experiments on rough inclined planes led to the development of the Pouliquen-Forterre rheology (PF), assuming a variable frictional behavior as a function of flow regime (i.e. Froude Number,  $Fr$ ) and flow depth (Pouliquen, 1999; Forterre and Pouliquen, 2002; Pouliquen and Forterre, 2002; Forterre and Pouliquen, 2003). They allowed for an improved modeling of front propagation, mass spreading, surface wave-propagation and vortices-evolution in the flows on a rough terrain (Forterre, 2006; Jop et al., 2006; Forterre and Pouliquen, 2008).

In parallel to and sometimes anticipating the earth avalanches experiments and models, study of snow avalanches led to the development of the Voellmy-Salm rheology (VS) (Voellmy, 1955; Salm et al., 1990; Salm, 1993; Bartelt et al., 1999). Dense snow or debris avalanches consist of mobilized, rapidly flowing ice-snow mixed to debris-rock granules (Bartelt and McArdell, 2009). The VS rheology assumes a velocity dependent resisting term in addition to the traditional basal friction, ideally capable of including an approximation of the turbulence-generated dissipation. Many experimental and theoretical studies were developed in this framework (Gruber and Bartelt, 2007; Kern et al., 2009; Christen et al., 2010; Fischer et al., 2012).

In Iverson (1997); Iverson and Denlinger (2001); Denlinger and Iverson (2001, 2004); Iverson et al. (2004), the depth-averaged model was further studied and applied in the simulation of test geophysical flows in large scale flume experiments. Moreover, Gray et al. (1999, 2003) tested modeling of fast avalanches, exploring the high-velocity effects of channelizing/chuting topographies. A compensation for the effect of earth pressure changes was implemented and explored in detail (Pirulli et al., 2007; Pirulli and Mangeney, 2008), as well as the implementation of a significant curvature in the terrain (Pudasaini and Hutter, 2003; Fischer et al., 2012). Several specific studies on the pore pressure effects on the flow initiation and fluidization were developed (Savage and Iverson, 2003; Iordanoff and Khonsari, 2004; Iverson and George, 2014). A two-phase model was also implemented to more accurately simulate heterogenous flows with a significant portion of interstitial fluid (Pitman and Le, 2005). *All of these complex modeling choices correspond to alternative or additional physical assumptions, and they are sometimes very difficult to evaluate, compare or reasonably combine together.*

A particular interest is raised by the specific efforts devoted to the modeling of volcanic mass flows with SWE (Freundt and Bursik, 1998; Pitman et al., 2003b; Bursik et al., 2005; Saucedo et al., 2005; Kelfoun and Druitt, 2005; Charbonnier and Gertisser, 2009; Kelfoun et al., 2009; Procter et al., 2010;

Sulpizio et al., 2010; Kelfoun, 2011; Charbonnier et al., 2013). Volcanoes are great sources for a rich variety of geophysical flow types and provide field data from past flow events.

In this study, we use the open source TITAN2D software for simulation of granular flows over natural terrains (represented by Digital Elevation Models (DEM)). TITAN2D solves depth-averaged equations using state of the art numerical methodology like adaptive mesh refinement, parallel computing (Pitman et al., 2003b; Patra et al., 2005, 2006; Yu et al., 2009), special methods for wet-dry interface capture (Aghakhani et al., 2016) and finds much use in hazard analysis of such flows using uncertainty quantification methods. The 4<sup>th</sup> release of TITAN2D offers multiple rheology options (MC, PF and VS rheologies) in the same computational platform. We leverage this capability and focus on modeling characteristics of these rheology options without concern for effects of diverse numerical methods. So far, TITAN2D achieved many successful applications in the simulation of different geophysical mass flows with specific characterisitics (Sheridan et al., 2005; Rupp et al., 2006; Norini et al., 2009; Charbonnier and Gertisser, 2009; Procter et al., 2010; Sheridan et al., 2010; Sulpizio et al., 2010; Capra et al., 2011). Several studies involving TITAN2D were recently directed towards a statistical study of geophysical flows, focusing on uncertainty quantification and propagation (Dalbey et al., 2008; Dalbey, 2009; Stefanescu et al., 2012a,b), or on the more efficient production of hazard maps (Bayarri et al., 2009; Spiller et al., 2014; Bayarri et al., 2015; Ogburn et al., 2016).

This study for the first time applies a statistical approach to the detailed investigation of the material model. Quantitative statistical analysis of *stress components* and their associated *powers*, as well as the *Froude Number Fr*, the *acceleration* and observable quantities as the flow *height*, *lateral extent*, and *area* over the full range of potential flows is obtained here. The stress components have a strong link with terms in the equations; moreover, the observable quantities have a direct link to field data and hazard assessments. *Our main purpose is to obtain a quantitative and statistical understanding of the consequences of the different physical assumptions, both on the forces inside the flow and on the observable outputs in time and space.*

In particular, what we present is a procedure for the improved exploration and quantitative comparison of physical models and their assumptions through the collection of full statistical data. Behind each physical model there are different physical assumptions, and therefore it is more appropriate to look at those instead than at the entire model results. Our statistical approach shall enable a first step towards a data driven selection of the best modeling assumptions to use.

## 2 Overview of the models

### 2.1 Modeling assumptions

The models of geophysical mass flows described in this study rely on several physical and mathematical assumptions. We will classify them in two groups - the general assumptions and the rheology assumptions. The main focus of this study is on the latter group, but, in principle, the same procedure could be applied to the former.

#### General Assumptions

- The *shallowness* approximation is at the base of the depth-averaging procedure. In this approximation, the flow depth is assumed to be at least an order of magnitude less than the characteristic length of the flowing material. Variation of velocity within the flow depth is neglected.
- The material is assumed to be *continuous*. The real flows consist of granular material and, often, interstitial fluid. Usually the “typical particle” diameter is small compared to the depth and length of the flowing mass, and the rheological properties are imposed to approximate the bulk behavior that is expected of an actual mass flow.
- The moving mass is assumed to be *volume preserving* and *incompressible*. In contrast, phenomena of erosion and deposition of material may violate this assumption.
- The body of mass is supposed to be in *isothermal* state or, if not, thermal effects can be ignored.
- The mass flow is assumed to be *free surface*. Air entrainment is instead frequently observed in the dilute real flows.

The shallowness assumption is very important, and brings several implications which may be considered additional assumptions on their own.

### Consequences of Shallowness

- The shallowness assumption implies a *hydrostatic* expression for the normal pressure in the direction perpendicular to the basal surface. Moreover, the downslope and cross-slope pressure components are assumed to be varying linearly with the normal pressure component through the flow depth.
- The *boundary layer* where the shearing deformation takes place is collapsed to zero thickness. The sliding and shearing velocity are combined to a single sliding law with a somewhat larger modelled sliding velocity.
- The *lateral shear stresses can be neglected*, compared to the basal shear stresses. Motion of the bulk of mass consists of “shearing within the deforming mass” and “sliding along the basal surface”.

The list rheology assumptions is detailed when the models are presented.

## 2.2 Governing equations and numerical solver

The motion of the mass flow is described by the basic conservation of mass and momentum for an incompressible medium:

$$\begin{aligned} \nabla \cdot \underline{\mathbf{u}} &= 0, \\ \frac{\partial}{\partial t}(\rho \underline{\mathbf{u}}) + \nabla \cdot (\rho \underline{\mathbf{u}} \otimes \underline{\mathbf{u}}) &= \nabla \cdot \underline{\mathbf{T}} + \rho \underline{\mathbf{g}}, \end{aligned} \quad (1)$$

Where  $\underline{\mathbf{u}} = [u, v, w]^T$  is the material velocity in cartesian coordinates,  $\rho$  is its constant density,  $\underline{\mathbf{T}}$  is the *Cauchy* stress tensor, and  $\underline{\mathbf{g}}$  is the gravity acceleration vector.

The Cauchy stress tensor,  $\underline{\mathbf{T}}$ , depends on the rheology assumptions. The kinetic boundary conditions are defined on the free surface  $F^s = s(x, y, t) - z = 0$  and basal surface  $F^b = b(x, y, t) - z = 0$  interfaces:

$$\frac{\partial F^s}{\partial t} + \underline{\mathbf{u}} \cdot \nabla F^s = 0, \quad \text{at } F^s(x, y, t) = 0 \quad (2)$$

$$\frac{\partial F^b}{\partial t} + \underline{\mathbf{u}} \cdot \nabla F^b = 0, \quad \text{at } F^b(x, y, t) = 0 \quad (3)$$

The depth-averaged Saint-Venant equations that TITAN2D solves are:

$$\begin{aligned} \frac{\partial h}{\partial t} + \frac{\partial}{\partial x}(h\bar{u}) + \frac{\partial}{\partial y}(h\bar{v}) &= 0, \\ \frac{\partial}{\partial t}(h\bar{u}) + \frac{\partial}{\partial x}\left(h\bar{u}^2 + \frac{1}{2}kg_z h^2\right) + \frac{\partial}{\partial y}(h\bar{u}\bar{v}) &= S_x, \\ \frac{\partial}{\partial t}(h\bar{v}) + \frac{\partial}{\partial x}(h\bar{u}\bar{v}) + \frac{\partial}{\partial y}\left(h\bar{v}^2 + \frac{1}{2}kg_z h^2\right) &= S_y \end{aligned} \quad (4)$$

Here the cartesian coordinate system is aligned such that  $z$  is normal to the surface;  $h$  is the flow height in the  $z$  direction;  $h\bar{u}$  and  $h\bar{v}$  are respectively the components of momentum in the  $x$  and  $y$  directions; and  $k$  is the coefficient which relates the lateral stress components,  $\bar{\sigma}_{xx}$  and  $\bar{\sigma}_{yy}$ , to the normal stress component,  $\bar{\sigma}_{zz}$ . The definition of this coefficient depends on the constitutive model of the flowing material we choose. Note that  $\frac{1}{2}kg_z h^2$  is the contribution of hydrostatic pressure to the momentum fluxes.  $S_x$  and  $S_y$  are the sum local stresses: they include the gravitational driving forces, the basal friction force resisting to the motion of the material, and additional forces specific of rheology assumptions.

Let  $\mathbf{U} = [h, h\bar{u}, h\bar{v}]^T$  be the vector of conservative variables and  $\mathbf{F} = [h\bar{u}, h\bar{u}^2 + 0.5k_{ap}g_z h^2, h\bar{v}\bar{u}]^T$  and  $\mathbf{G} = [h\bar{v}, h\bar{u}\bar{v}, h\bar{v}^2 + 0.5k_{ap}g_z h^2]^T$  be the physical flux vectors. In order to solve the system of hyperbolic conservation laws (4), TITAN2D employs a finite volume Godunov solver, and the time-stepping procedure is achieved by an explicit Euler scheme (Pitman et al., 2003b; Patra et al., 2005,

2006). Assuming  $\mathbf{S} = [S_h, S_x, S_y]^T$  as the source terms vector containing the effect of the flow rheology, the flow in the next time step updates as:

$$\mathbf{U}_{i,j}^{n+1} = \mathbf{U}_{i,j}^n - \frac{\Delta t}{\Delta x} \{ \mathbf{F}_{i+\frac{1}{2},j}^n - \mathbf{F}_{i-\frac{1}{2},j}^n \} - \frac{\Delta t}{\Delta y} \{ \mathbf{G}_{i,j+\frac{1}{2}}^n - \mathbf{G}_{i,j-\frac{1}{2}}^n \} + \Delta t \mathbf{S}_{i,j} \quad (5)$$

Where  $\mathbf{F}_{i\pm\frac{1}{2},j}^n$  and  $\mathbf{G}_{i,j\pm\frac{1}{2}}^n$  are the numerical flux terms at the inter-cell boundaries which are computed regarding the Harten-Lax-Van Leer Riemann solver (Toro, 2013). In fact, the evolution of the flow to the next time step depends on the advection flux at the cell interface, which results from the wave interaction at the boundaries between cells. On the other hand, adaptive mesh refinement allows for the concentration of computing power on regions of special interest. It captures the complex flow features along the flow boundaries, as well as the locations where there are large mass or momentum fluxes (which may include places where the topography changes abruptly). Mesh coarsening is also applied where the solution values are relatively constant or small to further improve the computational efficiency (Patra et al., 2005; Aghakhani et al., 2016).

## 2.3 Rheology assumptions

In the three following sections, we briefly describe *Mohr-Coulomb* (MC), *Pouliquen-Forsterre* (PF) and *Voellmy-Salm* (VS) models.

### 2.3.1 Mohr-Coulomb

Based on the long history of studies in soil mechanics (Rankine, 1857), the Mohr-Coulomb rheology model was developed and used to represent the behavior of geophysical mass flows Savage and Hutter (1989).

Shear and normal stress are assumed to obey Coulomb friction equation, both within the flow and at its boundaries. In other words,

$$\tau = \sigma \tan \phi, \quad (6)$$

where  $\tau$  and  $\sigma$  are respectively the shear and normal stresses on failure surfaces, and  $\phi$  is a friction angle. This relationship does not depend on the flow speed.

Under the assumption of symmetry of the stress tensor w.r.t. the  $z$  axis, the earth pressure coefficient  $k = k_{ap}$  can take on only one of three values indicated by the square dots shown in Figure 1. The material yield criterion is represented by the two straight lines at angles  $\pm\phi$  (the internal friction angle) relative to horizontal direction. Similarly, the normal and shear stress at the bed are represented by the line  $\tau = -\sigma \tan(\delta)$  where  $\delta$  is the bed friction angle. The three possible stress states in the  $xz$ -plane are indicated by the square dots. The circular dots show the additional possible stress states for  $\sigma_{yy}$  for a non-axisymmetric stress tensor.

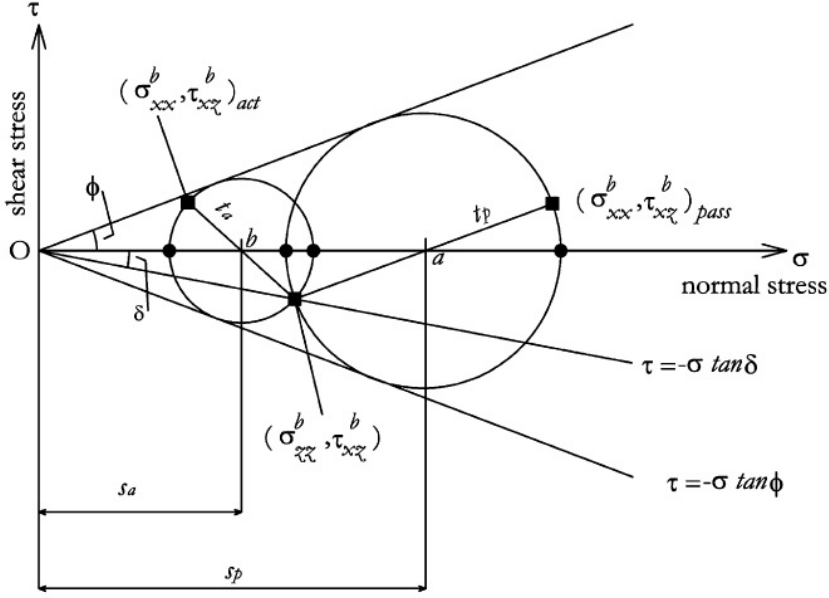


Figure 1: Mohr-circle-diagram representing the stress state within a granular medium (Pirulli et al., 2007).

Regarding the friction angle stated above, we have two material properties in this model:

- Internal friction angle,  $\phi_{int}$ , which resists material shear.
- Bed friction angle,  $\phi_{bed}$ , which resists motion of the material relative to the bed. This is a joint property of the material and the surface it flows over.

It is worth mentioning that the effective value of the friction angles can be strongly reduced by the presence of interstitial fluid, sometimes creating modeling issues. Specific models have been developed in case the effect of interstitial fluid is believed to be particularly relevant (Pitman and Le, 2005).

**Earth pressure coefficient**  $k = k_{ap}$  is defined in MC as:

$$k_{ap} = \begin{cases} \frac{\sigma_{xx}^{b\ act}}{\sigma_{zz}^b} = 2 \frac{1 - \sqrt{1 - \cos^2(\phi_{int})(1 + \tan^2(\phi_{bed}))}}{\cos^2(\phi_{int})} - 1, & \nabla \cdot \tilde{\mathbf{u}} > 0, \text{ active} \\ \frac{\sigma_{xx}^b}{\sigma_{zz}^b} = 1, & \nabla \cdot \tilde{\mathbf{u}} = 0, \text{ neutral} \\ \frac{\sigma_{xx}^{b\ pass}}{\sigma_{zz}^b} = 2 \frac{1 + \sqrt{1 - \cos^2(\phi_{int})(1 + \tan^2(\phi_{bed}))}}{\cos^2(\phi_{int})} - 1, & \nabla \cdot \tilde{\mathbf{u}} < 0, \text{ passive} \end{cases} \quad (7)$$

**MC equations** As a result, we can write down the source terms of the Eqs. (4):

$$\begin{aligned} S_x &= g_x h - \frac{\bar{u}}{\|\tilde{\mathbf{u}}\|} \left[ h \left( g_z + \frac{\bar{u}^2}{r_x} \right) \tan(\phi_{bed}) \right] - h k_{ap} \operatorname{sgn} \left( \frac{\partial \bar{u}}{\partial y} \right) \frac{\partial(g_z h)}{\partial y} \sin(\phi_{int}), \\ S_y &= g_y h - \frac{\bar{v}}{\|\tilde{\mathbf{u}}\|} \left[ h \left( g_z + \frac{\bar{v}^2}{r_y} \right) \tan(\phi_{bed}) \right] - h k_{ap} \operatorname{sgn} \left( \frac{\partial \bar{v}}{\partial x} \right) \frac{\partial(g_z h)}{\partial x} \sin(\phi_{int}) \end{aligned} \quad (8)$$

Where,  $\tilde{\mathbf{u}} = (\bar{u}, \bar{v})$ , is the depth-averaged velocity vector,  $r_x$  and  $r_y$  denote the radii of curvature of the local basal surface. The inverse of the radii of curvature is usually approximated with the partial derivatives of the basal slope, e.g.,  $1/r_x = \partial \theta_x / \partial x$ , where  $\theta_x$  is the local bed slope.

**MC rheology assumptions** In summary:

- *Basal Friction* is based on a constant friction angle.
- *Internal Friction* gives a not negligible contribution and it is based on a constant friction angle.
- *Earth pressure coefficient* formula depends on the Mohr-Coulomb circle.
- Velocity based *curvature effects* are included into the equations.

### 2.3.2 Pouliquen-Forterre

The scaling properties for granular flows down rough inclined planes led to a new formulation of the basal friction stress as a function of the flow depth and velocity (Pouliquen, 1999).

Two critical slope inclination angles are defined as functions of the flow thickness, namely  $\phi_{start}(h)$  and  $\phi_{stop}(h)$ . The function  $\phi_{stop}(h)$  gives the slope angle at which a steady uniform flow leaves a deposit of thickness  $h$ , while  $\phi_{start}(h)$  is the angle at which a layer of thickness  $h$  is mobilized. They define two different basal friction coefficients:

$$\mu_{start}(h) = \tan(\phi_{start}(h)) \quad (9)$$

$$\mu_{stop}(h) = \tan(\phi_{stop}(h)) \quad (10)$$

An empirical friction law  $\mu_b(\|\bar{\mathbf{u}}\|, h)$  is then defined in the whole range of velocity and thickness. The expression changes depending on two flow regimes, according to a parameter  $\beta$  and the Froude number  $Fr = \|\bar{\mathbf{u}}\| / \sqrt{hg_z}$ .

**Dynamic friction regime -  $Fr \geq \beta$**

$$\mu(h, Fr) = \mu_{stop}(h\beta/Fr) \quad (11)$$

**Intermediate friction regime -  $0 \leq Fr < \beta$**

$$\mu(h, Fr) = \left( \frac{Fr}{\beta} \right)^\gamma [\mu_{stop}(h) - \mu_{start}(h)] + \mu_{start}(h), \quad (12)$$

where  $\gamma$  is the power of extrapolation, assumed equal to  $10^{-3}$  in the sequel (Pouliquen and Forterre, 2002). In particular, if  $Fr = \beta$ , then  $\mu(h, Fr) = \mu_{stop}(h)$ , and if  $Fr = 0$ , then  $\mu(h, Fr) = \mu_{start}(h)$ .

The functions  $\mu_{stop}$  and  $\mu_{start}$  are defined by:

$$\mu_{stop}(h) = \tan \phi_1 + \frac{\tan \phi_2 - \tan \phi_1}{1 + h/\mathcal{L}} \quad (13)$$

and

$$\mu_{start}(h) = \tan \phi_3 + \frac{\tan \phi_2 - \tan \phi_1}{1 + h/\mathcal{L}} \quad (14)$$

The critical angles  $\phi_1$ ,  $\phi_2$  and  $\phi_3$  and the parameters  $\mathcal{L}, \beta$  are the parameters of the model.

In particular,  $\mathcal{L}$  is the characteristic depth of the flow over which a transition between the angles  $\phi_1$  to  $\phi_2$  occurs, in the  $\mu_{stop}$  formula. In practice, if  $h \ll \mathcal{L}$ , then  $\mu_{stop}(h) \approx \tan \phi_2$ , and if  $h \gg \mathcal{L}$ , then  $\mu_{stop}(h) \approx \tan \phi_1$ . The effect of the topographic local curvatures is also taken into account.

**PF equations** The depth-averaged Eqs. (4) source terms thus take the following form:

$$\begin{aligned} S_x &= g_x h - \frac{\bar{u}}{\|\bar{\mathbf{u}}\|} \left[ h \left( g_z + \frac{\bar{u}^2}{r_x} \right) \mu_b(\|\bar{\mathbf{u}}\|, h) \right] + g_z h \frac{\partial h}{\partial x} \\ S_y &= g_y h - \frac{\bar{v}}{\|\bar{\mathbf{u}}\|} \left[ h \left( g_z + \frac{\bar{v}^2}{r_y} \right) \mu_b(\|\bar{\mathbf{u}}\|, h) \right] + g_z h \frac{\partial h}{\partial y} \end{aligned} \quad (15)$$

**PF rheology assumptions** In summary:

- *Basal Friction* is based on an interpolation of different friction angles, based on the flow regime and depth.
- *Internal Friction* is neglected.
- *Earth pressure coefficient* is equal to one.
- Normal stress is modified by a *hydrostatic pressure force* related to the flow height gradient.
- Velocity based *curvature effects* are included into the equations.

### 2.3.3 Voellmy-Salm

The theoretical analysis of dense snow avalanches led to the VS rheology model (Voellmy, 1955; Salm, 1993). The following relation between shear and normal stresses holds:

$$\tau = \mu\sigma + \frac{\rho\|\underline{\mathbf{g}}\|}{\xi}\|\tilde{\underline{\mathbf{u}}}\|^2, \quad (16)$$

where,  $\sigma$  denotes the normal stress at the bottom of the fluid layer and  $\underline{\mathbf{g}} = (g_x, g_y, g_z)$  represents the gravity vector. The VS rheology adds a velocity dependent *turbulent friction* to the traditional velocity independent basal friction term which is proportional to the normal stress at the flow bottom. The two parameters of the model are the bed friction coefficient  $\mu$  and the turbulent friction coefficient  $\xi$ . By dimension analysis,  $\xi$  is equivalent to an acceleration, while  $\mu$  is dimensionless. The decomposition of the total basal friction into velocity independent and dependent parts allows the modeling of either the dynamic regime when the avalanche is flowing with a high velocity in the acceleration zone, and when it is close to stopping in the runout zone.

The effect of the topographic local curvatures is again taken into account by adding the terms containing the local radii of curvature  $r_x$  and  $r_y$ . In this case the formula is considering the modulus of velocity instead than the scalar component (Fischer et al., 2012).

**VS equations** Therefore, the final source terms take the following form:

$$\begin{aligned} S_x &= g_x h - \frac{\bar{u}}{\|\tilde{\underline{\mathbf{u}}}\|} \left[ h \left( g_z + \frac{\|\tilde{\underline{\mathbf{u}}}\|^2}{r_x} \right) \mu + \frac{\|\underline{\mathbf{g}}\|}{\xi} \|\tilde{\underline{\mathbf{u}}}\|^2 \right], \\ S_y &= g_y h - \frac{\bar{v}}{\|\tilde{\underline{\mathbf{u}}}\|} \left[ h \left( g_z + \frac{\|\tilde{\underline{\mathbf{u}}}\|^2}{r_y} \right) \mu + \frac{\|\underline{\mathbf{g}}\|}{\xi} \|\tilde{\underline{\mathbf{u}}}\|^2 \right]. \end{aligned} \quad (17)$$

**VS rheology assumptions** In summary:

- *Basal Friction* is based on a constant coefficient, similarly to the MC rheology.
- *Internal Friction* is neglected.
- *Earth pressure coefficient* is equal to one.
- Additional *turbulent friction* is based on the local velocity by a quadratic expression.
- Velocity based *curvature effects* are included into the equations, following an alternative formulation.

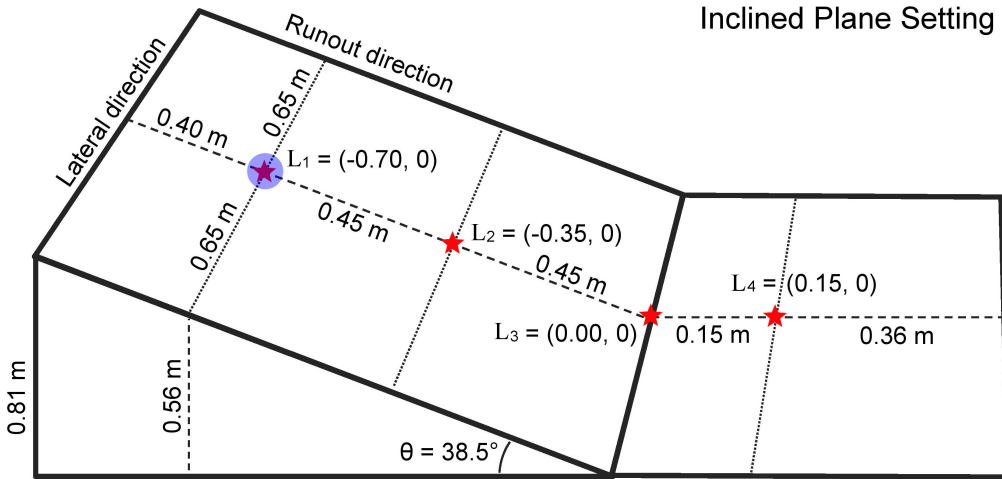


Figure 2: Inclined plane description, including local samples sites (red stars). Pile location is marked by a blue dot.

## 2.4 Overview of the case studies

The first case study assumes very simple boundary conditions, and corresponds to an experiment fully described in Webb (2004); Bursik et al. (2005); Webb and Bursik (2016). It is a classical flow down an inclined plane set-up, including a change in slope to an horizontal plane (Fig. 2). Four locations are selected among the center line of the flow to accomplish local testing. These are: the initial pile location  $L_1 = (-0.7, 0)$  m, the middle of the inclined plane  $L_2 = (-0.35, 0)$  m, the change in slope  $L_3 = (0, 0)$  m, the middle of the flat plane  $L_4 = (0.15, 0)$  m (see Section 4).

The second case study is a block and ash flow down the slope of Volcán de Colima (MX) - an andesitic stratovolcano that rises to 3,860 m above sea level, situated in the western portion of the Trans-Mexican Volcanic Belt (Fig. 3). Historically, it has been the most active volcano in México (la Cruz-Reyna, 1993; Zobin et al., 2002; González et al., 2002). The modeling of pyroclastic flows generated by explosive eruptions and lava dome collapses of Volcán de Colima is a well studied problem (Martin Del Pozzo et al., 1995; Sheridan and Macías, 1995; Saucedo et al., 2002, 2004, 2005; Sarocchi et al., 2011; Capra et al., 2015). The presence of a change in slope followed by multiple ravines characterize this framework. The volcano has been already used as a case study in several research involving the Titan2D code (Rupp, 2004; Rupp et al., 2006; Dalbey et al., 2008; Yu et al., 2009; Sulpizio et al., 2010; Capra et al., 2011; Aghakhani et al., 2016). During July 10<sup>th</sup>-11<sup>th</sup>, 2015, the volcano underwent its most intense eruptive phase since its Subplinian-Plinian 1913 AD eruption (Saucedo et al., 2010; Zobin et al., 2015; Reyes-Dávila et al., 2016; Capra et al., 2016; Macorps et al., 2018).

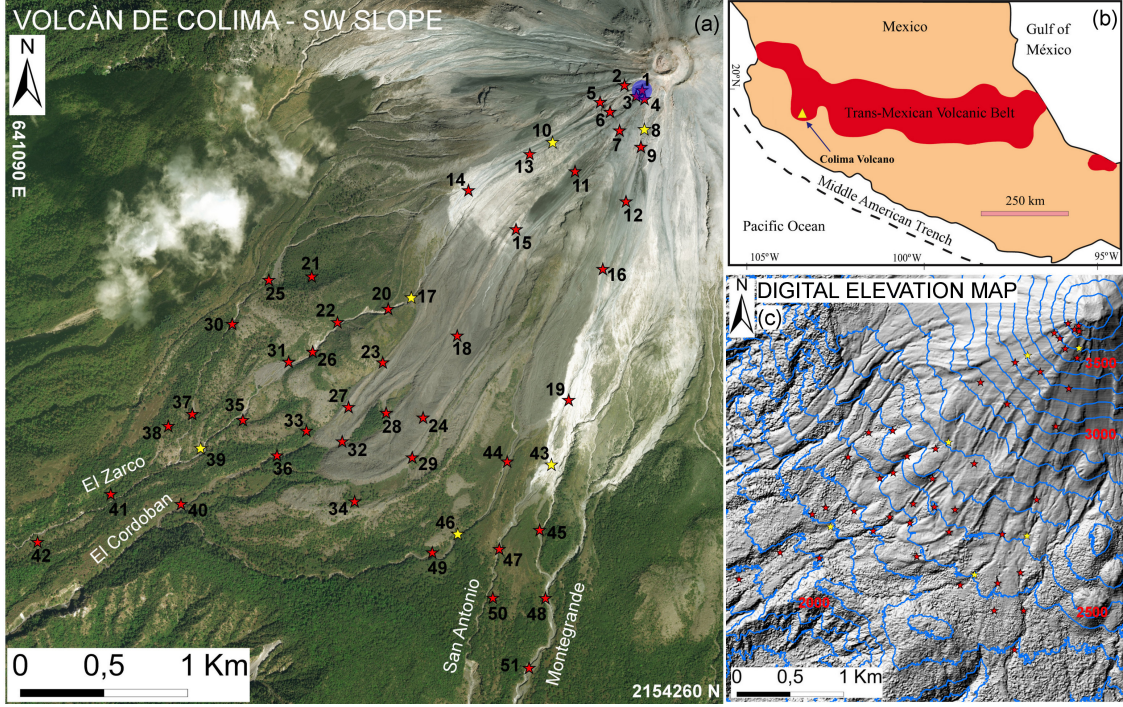


Figure 3: (a) Volcán de Colima (Méjico) overview, including 51 numbered local sample sites (stars) and four labeled major ravines channeling the flow. Pile location is marked by a blue dot. Reported coordinates are in UTM zone 13N. Background is a satellite photo. (b) Regional geology map. (c) Digital elevation map. Six points that are adopted as preferred locations are highlighted in yellow. Elevation isolines are included in blue, elevation values in red.

We assume the flow to be generated by the gravitational collapse of a material pile placed close to the summit area. The volcano already produced either pyroclastic flows generated by lava dome collapse, called Merapi style flows, or by an eruptive column partial collapse, i.e. Soufrière style flows (Macorps et al., 2018). A dome collapse occurs when there is a significant amount of recently-extruded highly-viscous lava piled up in an unstable configuration around a vent. Further extrusion and/or external forces can cause the still hot dome of viscous lava to collapse, disintegrate, and avalanche downhill (Bursik et al., 2005; Wolpert et al., 2016; Hyman and Bursik, 2018). Eruptive column collapse can occur during explosive eruptions, when the eruption column can no longer sustain the weight of material due to loss of pressure, and hence it partially collapses down. The hot, dense blocks in this “block and ash” flow (BAF) will typically range from centimeters to a few meters in size. The matrix is composed of fine ash from the comminuted blocks. Computations were performed on a DEM with 5m-pixel resolution, obtained from LiDAR data acquired in 2005 (Davila et al., 2007; Sulpizio et al., 2010). We placed 51 locations along the flow inundated area to accomplish local testing. Six of them are then adopted as preferred locations, being representative of different flow regimes.

### 3 Uncertainty quantification process

#### 3.1 General formulation

The key to a good forecasting capability in the context of mass flows requires the careful selection of the pair  $(M(A), P_{M(A)})$ , where  $A$  is a set of assumptions,  $M(A)$  is the model which combines those assumptions, and  $P_M$  is a probability distribution in the parameter space of  $M$ . For the sake of simplicity we are always taking  $P_M$  uniformly distributed on selected parameter ranges.

**Models and assumptions** An assumption is a quite general concept - for example it can be a specific equation for the internal stress, the implementation of bed curvature effects, of active-passive material stretching, or the use of a specific correction on the pressure effects. Assumptions are what makes the models being different, and each model may be seen as the combined result of a set of assumptions. Sometimes a good model contains a useless assumption that may be removed, sometimes a good assumption should be implemented inside a different model - those are usually considered as subjective choices, not data driven. Moreover, the correct assumptions may change through time, making the analysis more difficult. We provided a list of assumptions behind SWE general implementation, and behind each rheology in section 2.

**Parameters ranges** It is worth mentioning that whereas the support of  $P_M$  can be restricted to a single point in case an inverse problem is solved for the optimal reconstruction of a particular flow, this is not possible if we are interested in the general predictive capabilities of the model, i.e. the target of probabilistic hazard assessment. In this study we always assume  $P_M \sim \bigotimes_{i=1}^{N_M} Unif(a_{i,M}, b_{i,M})$ , where  $N_M$  is the number of parameters of  $M$ . These parameter ranges will not be selected under the influence of a particular observation, but we will try to use the information gathered in literature about the physical meaning of those values, together with a preliminary testing, aligning the range of possible runouts. This alignment step is detailed in section 3.3, and required to focus the statistical comparison on a consistence range of flow regimes.

**Simulated quantities** The simulation algorithms can be schematized as:

$$(1) \text{INPUT VARIABLES} \rightarrow (2) \text{DYNAMIC QUANTITIES} \rightarrow (3) \text{OBSERVABLE OUTPUTS}$$

The *input variables* are the parameters of  $M$ , i.e. volume, rheology coefficients, but can include also the initiation site and geometry, and the digital elevation map. The *dynamic quantities* include the stress terms in the Newton Equations that rule the simulation, and their powers. Those are hidden to the observation in a real flow, but they directly depend on the parameters, and represent a fundamental link between the parameters and the observable outputs. Moreover, the models share some of those terms while change others, and this enables a detailed comparison of the real physics below the curtain (see Sections 4.2, 5.3). Finally, the *observable outputs* include what can be measured in space and time: e.g. flow height, lateral extent, area, velocity, acceleration, and combined quantities as  $Fr$  (see Sections 4.1, 5.2). In the sequel (2) and (3) are also called quantities of interest (QoI).

**Monte Carlo simulation** In general, for each QoI, during a Monte Carlo simulation we sample the input variables and obtain a family of temporal graphs on time domains depending on the flow duration. These results are statistically summarized - plotting their expectation, and their 5<sup>th</sup> and 95<sup>th</sup> percentiles. In the following, we will detail the considered input variables and quantities of interest for each of our cases study.

Our sampling technique of the input variables is based on the Latin Hypercube Sampling (LHS) idea, and in particular, on the improved space-filling properties of the orthogonal array-based Latin Hypercubes (see Appendix A). The LHS is performed over  $[0, 1]^3$  for the MC and VS input parameters, and  $[0, 1]^4$  for PF input parameters (see Section 3.3). Those adimensional samples are translated and linearly scaled to fill the required intervals.

**Local samples and spatial averaging** The QoI in the previous scheme which are evolving fields  $f(\underline{\mathbf{x}}, t)$  in space-time, can be either *locally sampled* or *spatially integrated* (see sections 4, 5). The spatial integral is defined by  $F(t) = \int_{\mathbb{R}^k} f(\underline{\mathbf{x}}, t) d\underline{\mathbf{x}}$ . In the most of the cases  $k = 2$ , and  $d\underline{\mathbf{x}}$  is given by the area of the mesh elements. Sometimes  $k = 3$ , e.g. concerning speed, and  $d\underline{\mathbf{x}}$  is the element of volume corresponding to the mesh elements.

A fundamental part of this research was made possible by the new implementation of a local sampling option in the TITAN2D cyber-infrastructure. In particular, once a set of sample points  $(x_i)_{i=1,\dots,N}$  is chosen, each field  $f(\underline{\mathbf{x}}, t)$  is calculated as a function of time on the elements of the numerical mesh which are found to contain the  $(x_i)_{i=1,\dots,N}$ . Exploring differences in time and location enable to constrain the changes in flow regime. Those are really important because if the flow behavior is radically different, then the significance and effects of the assumptions may also change.

**Statistical analysis of dynamical quantities** Let  $(F_i(x, t))_{i=1,\dots,4}$  be an array of force components, where  $x \in \mathbb{R}^2$  is a spatial location, and  $t \in T$  is a time instant. The degree of contribution of those force terms can be significantly variable in space and time, and we define the *dominance factors*  $(p_j)_{j=1,\dots,k}$ , i.e. the probability of each  $F_j$  to be the dominant force at  $(x, t)$ . Those probabilities tell what is chance of being the greater force term, and hence can provide a concise statistical description of the model dynamics. The dominance factors can be adopted to define a statistical decomposition of the contributions of the forces, as detailed in Appendix B. In sections 4.2.2 and 5.3.2 we report the dominance factors plots, to read the dynamic significance of the forces as a function of time and location.

### 3.2 Forces terms definition

Forces analyzed have been classified according to the terms of the momentum equation in (4). Moreover, the forces terms in  $S_x$  have been additionally classified, accordingly to equations (8), (15), (17), describing the three rheology models considered in this study. What follows is a summary of the force terms, and this notation will be used in the following (see Sections 4.2, 5.3). In our case study, we focus on the right-hand side terms in the momentum equation. The analysis of *RHS* will inform on local effects, while focusing instead on the *LHS* would concern the exploration of global dynamics in space and time.

**Left-hand side, LHS forces** These terms are not detailed further in this study, but are included for the sake of completeness.

$$\mathbf{LHS}_1 = \left[ \frac{\partial}{\partial t}(h\bar{u}), \frac{\partial}{\partial t}(h\bar{v}) \right], \quad (18)$$

it is the temporal derivative of momentum.

$$\mathbf{LHS}_2 = \left[ \frac{\partial}{\partial x} \left( h\bar{u}^2 + \frac{1}{2}kg_z h^2 \right) + \frac{\partial}{\partial y}(h\bar{u}\bar{v}), \frac{\partial}{\partial x}(h\bar{u}\bar{v}) + \frac{\partial}{\partial y} \left( h\bar{v}^2 + \frac{1}{2}kg_z h^2 \right) \right], \quad (19)$$

it is the material derivative of momentum, due to the advection.

**Right-hand side, RHS forces** These terms are explored in detail in the next sections.

$$\mathbf{RHS}_1 = [g_x h, g_y h], \quad (20)$$

it is the gravitational force term, it has the same formulation in all models.

The formula of basal friction force  $\mathbf{RHS}_2$  depends on the model:

$$\begin{aligned} \mathbf{RHS}_2 &= -hg_z \tan(\phi_{bed}) \left[ \frac{\bar{u}}{\|\tilde{\mathbf{u}}\|}, \frac{\bar{v}}{\|\tilde{\mathbf{u}}\|} \right], \text{ in MC model.} \\ \mathbf{RHS}_2 &= -hg_z \mu_b(\|\tilde{\mathbf{u}}\|, h) \left[ \frac{\bar{u}}{\|\tilde{\mathbf{u}}\|}, \frac{\bar{v}}{\|\tilde{\mathbf{u}}\|} \right], \text{ in PF model.} \\ \mathbf{RHS}_2 &= -hg_z \mu \left[ \frac{\bar{u}}{\|\tilde{\mathbf{u}}\|}, \frac{\bar{v}}{\|\tilde{\mathbf{u}}\|} \right], \text{ in VS model.} \end{aligned} \quad (21)$$

The formula of the force related to the topography curvature,  $\mathbf{RHS}_3$ , also depends on the model:

$$\begin{aligned} \mathbf{RHS}_3 &= -h \tan(\phi_{bed}) \left[ \frac{\bar{u}^3}{r_x \|\tilde{\mathbf{u}}\|}, \frac{\bar{v}^3}{r_y \|\tilde{\mathbf{u}}\|} \right], \text{ in MC model.} \\ \mathbf{RHS}_3 &= -h \mu_b(\|\tilde{\mathbf{u}}\|, h) \left[ \frac{\bar{u}^3}{r_x \|\tilde{\mathbf{u}}\|}, \frac{\bar{v}^3}{r_y \|\tilde{\mathbf{u}}\|} \right], \text{ in PF model.} \\ \mathbf{RHS}_3 &= -h \mu \left[ \frac{\bar{u} \|\tilde{\mathbf{u}}\|}{r_x}, \frac{\bar{v} \|\tilde{\mathbf{u}}\|}{r_y} \right], \text{ in VS model.} \end{aligned} \quad (22)$$

All the three models have an additional force term, having a different formula and meaning in the three models:

$$\begin{aligned}
\mathbf{RHS}_4 &= -hk_{ap} \sin(\phi_{int}) \left[ \operatorname{sgn}\left(\frac{\partial \bar{u}}{\partial y}\right) \frac{\partial(g_z h)}{\partial y}, \operatorname{sgn}\left(\frac{\partial \bar{v}}{\partial x}\right) \frac{\partial(g_z h)}{\partial x} \right], \text{ in MC model.} \\
\mathbf{RHS}_4 &= g_z h \left[ \frac{\partial h}{\partial x}, \frac{\partial h}{\partial y} \right], \text{ in PF model.} \\
\mathbf{RHS}_4 &= -\frac{\|\mathbf{g}\|}{\xi} \|\tilde{\mathbf{u}}\|^2 \left[ \frac{\bar{u}}{\|\tilde{\mathbf{u}}\|}, \frac{\bar{v}}{\|\tilde{\mathbf{u}}\|} \right], \text{ in VS model.}
\end{aligned} \tag{23}$$

### 3.3 Alignment and consistency of the input ranges

In general, the three rheologies considered in this study, MC, PF, and VS, have totally different parameters. The statistical testing that we perform requires to choose the parameter range  $P_M$ , and in principle it may be arbitrary. Nevertheless, if the total frictions of the models were not covering a similar span, the statistical comparison would be dominated by trivial macroscopic differences, and could not focus on the rheology details. Some degree of parameter consistency is hence required between the models.

We can find several instances of parameter choices in literature, and in general these choices appear to depend on the case study. In all the models it is defined a basal friction stress (see  $RHS_2$  in 4). However, PF interpolates different effective friction angles, while VS includes a speed dependent additional term. We found that a direct consistency of effective friction angles is problematic to impose globally. Hence, we did not follow such approach. Instead, we made a preliminary testing on the extreme values of the parameter space, i.e. matching the runouts of ***max volume – min resistance***, and ***min volume – max resistance***.

**General definitions** We assume what follows to simplify testing. Except when differently specified, parameters are uniformly sampled in linear scale.

- Material Volume  $V$  is an additional input parameter in all the models, on a fixed range.
- In MC, sampled input parameters are  $\phi_{bed}$ , and  $\Delta\phi := \phi_{int} - \phi_{bed}$ . In particular,  $\Delta\phi \in [2^\circ, 10^\circ]$  (Dalbey et al., 2008).
- In PF, sampled input parameters are  $\phi_1$ ,  $\Delta\phi_{12} := \phi_2 - \phi_1$ , and  $\beta$ . In particular,  $\Delta\phi_{12} \in [10^\circ, 15^\circ]$ , and  $\beta \in [0.1, 0.85]$ . Moreover,  $\phi_3 = \phi_1 + 1^\circ$ , and  $\mathcal{L}$  is equal to 1 dm and 1 mm in the two case studies, respectively (Pouliquen and Forterre, 2002; Forterre and Pouliquen, 2003; Gray and Edwards, 2014; Barker et al., 2015).
- In VS, sampled input parameters are  $\mu$ , and  $\xi$ . In detail,  $\xi$  uniform sampling is accomplished in log-scale. In fact, values of  $\xi$  between 250 and 4,000  $m/s^2$  have been described for snow avalanches (Salm, 1993; Bartelt et al., 1999; Gruber and Bartelt, 2007).

In summary, MC and VS have three-dimensional parameter spaces, while PF a four-dimensional parameter space.

**Flow down an inclined plane** In this case study, Dalbey et al. (2008) assumed  $\phi_{bed} = [15^\circ, 30^\circ]$ , while Webb and Bursik (2016) performed a series of laboratory experiments and found  $\phi_{bed} = [18.2^\circ, 34.4^\circ]$ . We relied on those published parameter choices to decide a comprehensive parameter range. Figure 4 displays the maps of max flow height and max velocities observed in the extreme cases tested. Simulation options are - `max_time = 2 s`, `height/radius = 1.34`, `length_scale = 1 m`, `number_of_cells_across_axis = 10`, `order = first`, `geoflow_tiny = 1e4` (Patra et al., 2005; Aghakhani et al., 2016). Initial pile geometry is cylindrical.

- **Material Volume:**  $[449.0, 607.0] \text{ cm}^3$ , i.e. average of  $528.0 \text{ cm}^3$  and uncertainty of  $\pm 15\%$ .

- **Rheology models' parameter space:**

The parameter ranges adopted in this case study are:

**MC** -  $\phi_{bed} \in [18^\circ, 30^\circ]$ .

**PF** -  $\phi_1 \in [10^\circ, 22^\circ]$ .

**VS** -  $\mu \in [0.22, 0.45]$ ,  $\log(\xi) \in [3, 4]$ .

Even if maximum and minimum runout are both matching, the shape and lateral extent of the flow is remarkably different in the maximum runout case, according to the three models. In particular, MC model can produce the largest lateral extent, and VS model displays an accentuated bow-like shape, due to the increased friction in the lateral margins.

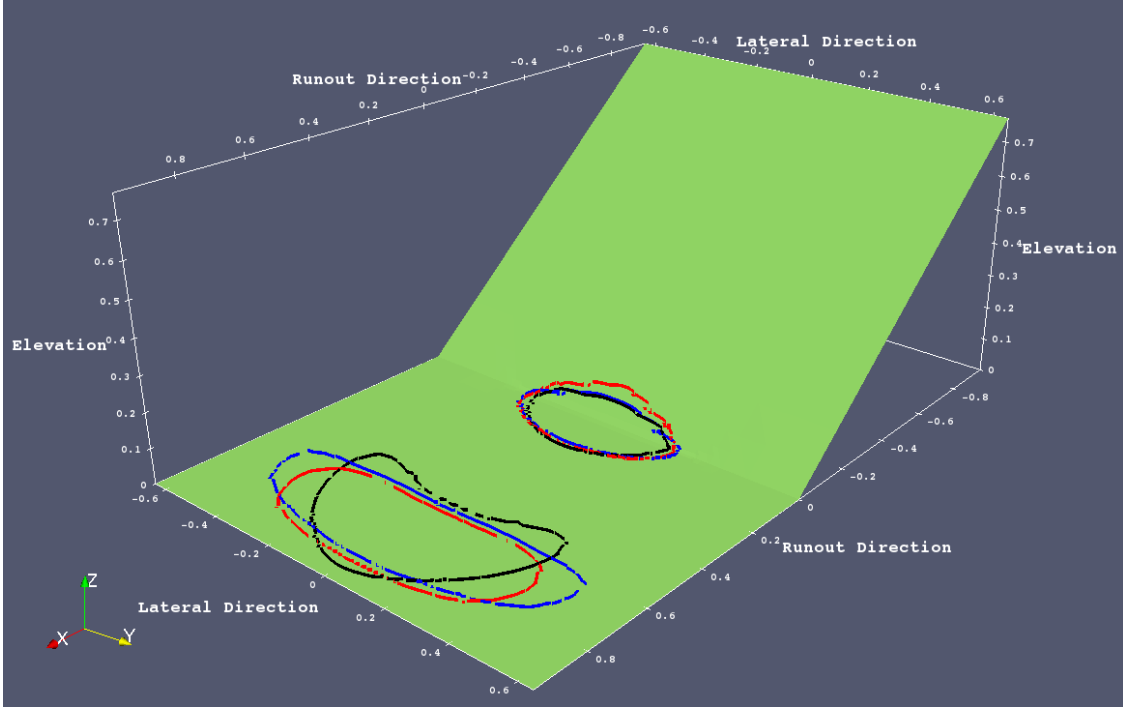


Figure 4: Inclined plane setup. Contours of  $h = 1.0 \text{ mm}$  at last simulated snapshot ( $t = 1.5 \text{ sec}$ ) for simulated flows with *minimum runout* obtained from **min volume – max resistance**, and *maximum runout* obtained from **max volume – min resistance**. — : MC, — : PF, — : VS.

**Volcán de Colima block and ash flow** In this case study, [Dalbey et al. \(2008\)](#) assumed  $\phi_{bed} = [15^\circ, 35^\circ]$ , while ([Capra et al., 2011](#)) adopted  $\phi_{bed} = 30^\circ$  in the simulation of a BAF in that same setting. Moreover, [Spiller et al. \(2014\)](#); [Bayarri et al. \(2015\)](#); [Ogburn et al. \(2016\)](#) found a statistical correlation between flow size and effective basal friction inferred from field observation of geophysical flows. The size of the BAF of this study would have  $\phi_{bed} = [13^\circ, 18^\circ]$  according to their estimates. Figure 5 displays the maps of max flow height and max velocities observed in the extreme cases tested. Simulation options are - max.time = 7200 s (2 hours), height/radius = 0.55, length\_scale = 4e3 m, number\_of\_cells\_across\_axis = 50, order = first, geoflow\_tiny = 1e4 ([Patra et al., 2005](#); [Aghakhani et al., 2016](#)). Initial pile geometry is paraboloid.

- **Material Volume:**  $[2.08, 3.12] \times 10^5 \text{ m}^3$ , i.e. average of  $2.6 \times 10^5 \text{ m}^3$  and uncertainty of  $\pm 20\%$ .
- **Rheology models' parameter space:**

The parameter ranges adopted in this case study are:

$$\mathbf{MC} - \phi_{bed} \in [10^\circ, 25^\circ].$$

$$\mathbf{PF} - \phi_1 \in [8^\circ, 18^\circ].$$

$$\mathbf{VS} - \mu \in [0.15, 0.45], \quad \log(\xi) \in [1.7, 4].$$

The models possess different features, but the maximum runout after channelization in the ravines is matching. In particular, VS lateral spreading is significant lower and the material reaches higher thickness, whereas PF model seems to stop more gradually than MC with a more complex inundated area boundary lines. These features are the macroscopic consequence of the rheology differences.

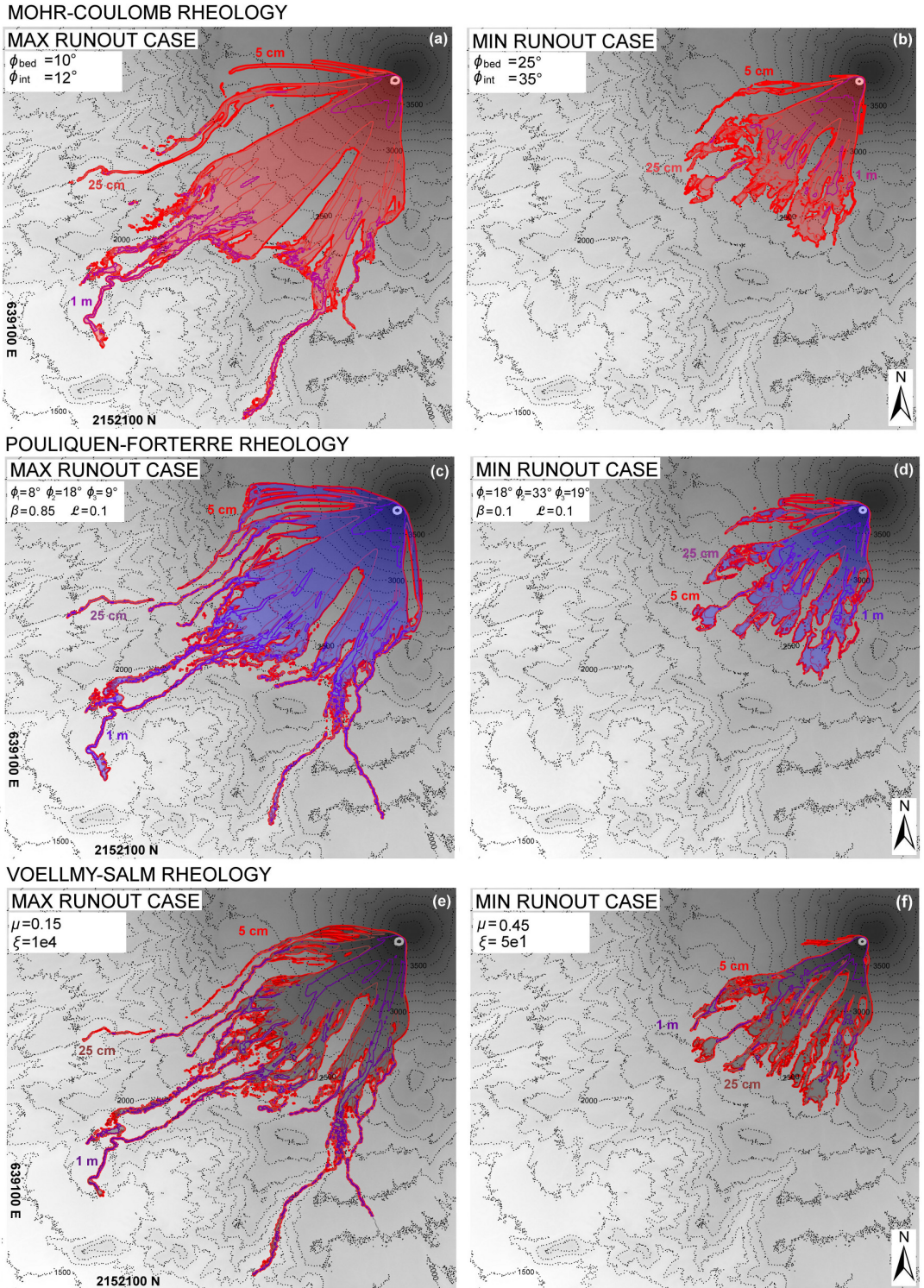


Figure 5: Volcán de Colima BAF. Comparison between *max flow height* maps of simulated flow, assuming Mohr-Coulomb (a),(b), Pouliquen-Forterre (c),(d), and Voellmy-Salm (e),(f) rheology. Extreme cases producing maximum and minimum runout, i.e. (a),(c),(e) **max volume – min resistance** and (b),(d),(f) **min volume – max resistance**.

## 4 Results of small scale flows on inclined plane and flat runway

This case study is a small scale experimental setting. First we describe the observable outputs (Section 4.1), and then the hidden dynamic quantities (Section 4.2). In many plots we note the effect of cutting the flow when height is  $< 1$  mm, which is at the scale of the smallest granular size. In fact, continuity assumption would not be valid below this scale. In particular, in Fig. 6 both the 5<sup>th</sup> and 95<sup>th</sup> percentile plots are vertically cut to zero when they decrease over that threshold. The mean plot is not cut to zero but it is dulled by this cutoff.

### 4.1 Observable outputs

Observable outputs include the flow height and acceleration as a function of time, measured in the four locations  $L_1, \dots, L_4$  displayed in Fig. 2. In addition, lateral extension, flow area, and spatially averaged speed and  $Fr$  are displayed. Uncertainty quantification (UQ) is always performed, accordingly to the parameter ranges described in Section 3.3. Locally measured Froude Number is included in Supporting Information S1.

#### 4.1.1 Flow height

Figure 6 shows the flow height,  $h(L, t)$ , at the points  $(L_i)_{i=1,\dots,4}$ , for the three rheology models.

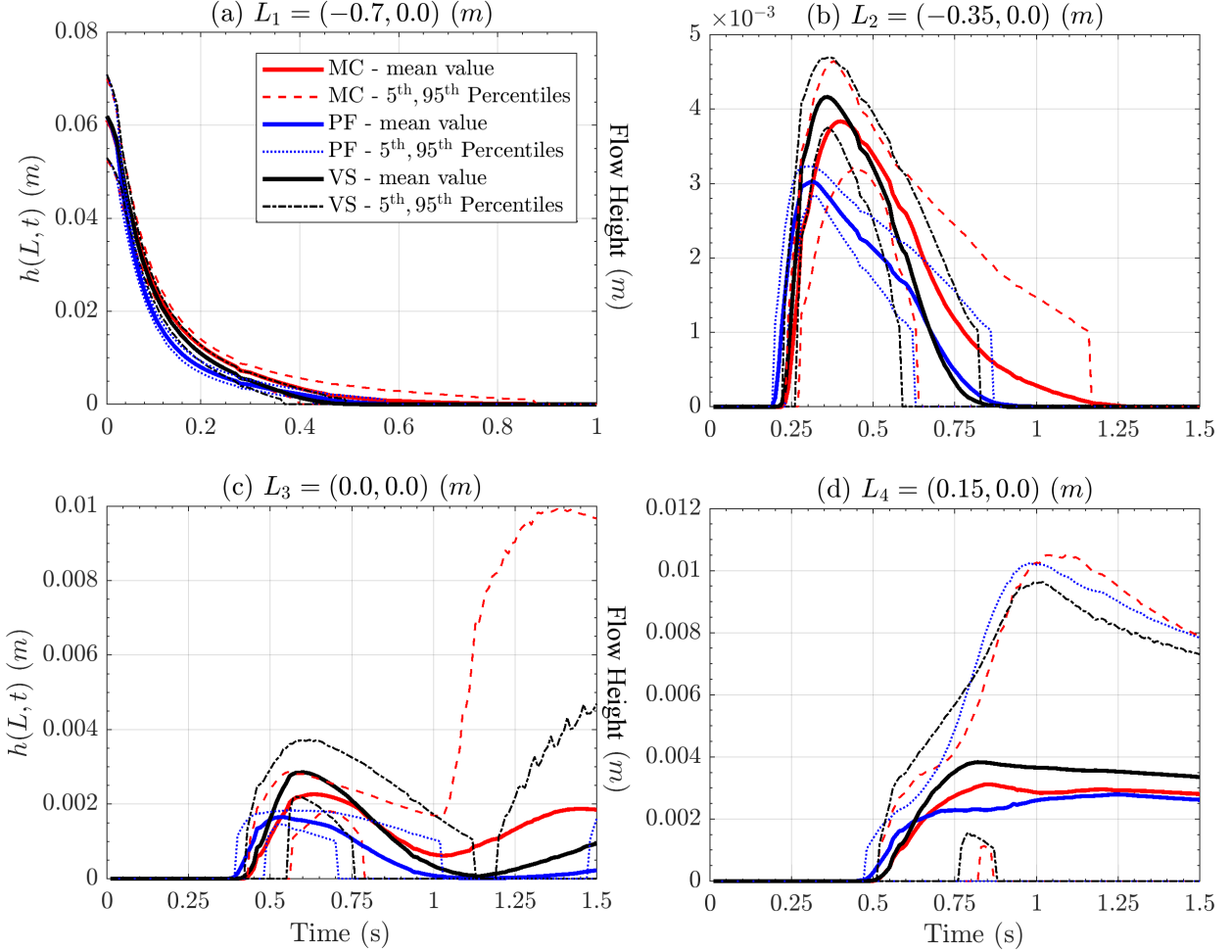


Figure 6: Records of flow height at four spatial locations of interest. Bold line is mean value, dashed/dotted lines are 5<sup>th</sup> and 95<sup>th</sup> percentile bounds. Different rheology models are displayed with different colors. Plots are at different scale, for simplifying lecture.

In plot 6a, related to point  $L_1$  placed on the initial pile, the initial values of  $\sim 6 \pm 1$  cm are the equal and express the assigned pile height. The flow height decreases slightly faster in PF model, and slower in MC, compared to VS. Differences are more significant in plot 6b, related to point  $L_2$ , placed in the middle of the slope. Maximum flow height on average is greater in VS,  $4.1 \pm 0.2$  mm, but more uncertain in MC,  $3.9 \pm 0.4$  mm, and generally smaller in PF model,  $3.0 \pm 0.1$  mm. After the peak, PF decreases significantly slower than the other models. These height values are about 15 times smaller than initial pile height. None of the models leaves a significant material deposit in  $L_1$  or  $L_2$ , and hence the 95<sup>th</sup> percentile of the height is null at the ending-time. In contrast, a deposit is left at points  $L_3$  and  $L_4$ , i.e. plot 6c placed at the change in slope, and plot 6d in the middle of the flat runout. At  $L_3$  MC's deposit, 2 mm with uncertainty [-2,+8] mm, is higher than the other models'. The plot profile is bimodal, showing a first peak at  $\sim 0.6$  s, and then a reduction until 1 s, before the final accumulation. At  $L_4$ , deposit it is not significantly different between the three models. It measures  $\sim 3$  mm on average, slightly more than this in VS, with uncertainty [-3,+7] mm.

#### 4.1.2 Flow acceleration

Figure 7 shows the flow speed,  $\|\underline{\mathbf{a}}\|(L, t)$ , at the points  $(L_i)_{i=1,\dots,4}$ , for the three rheology models.

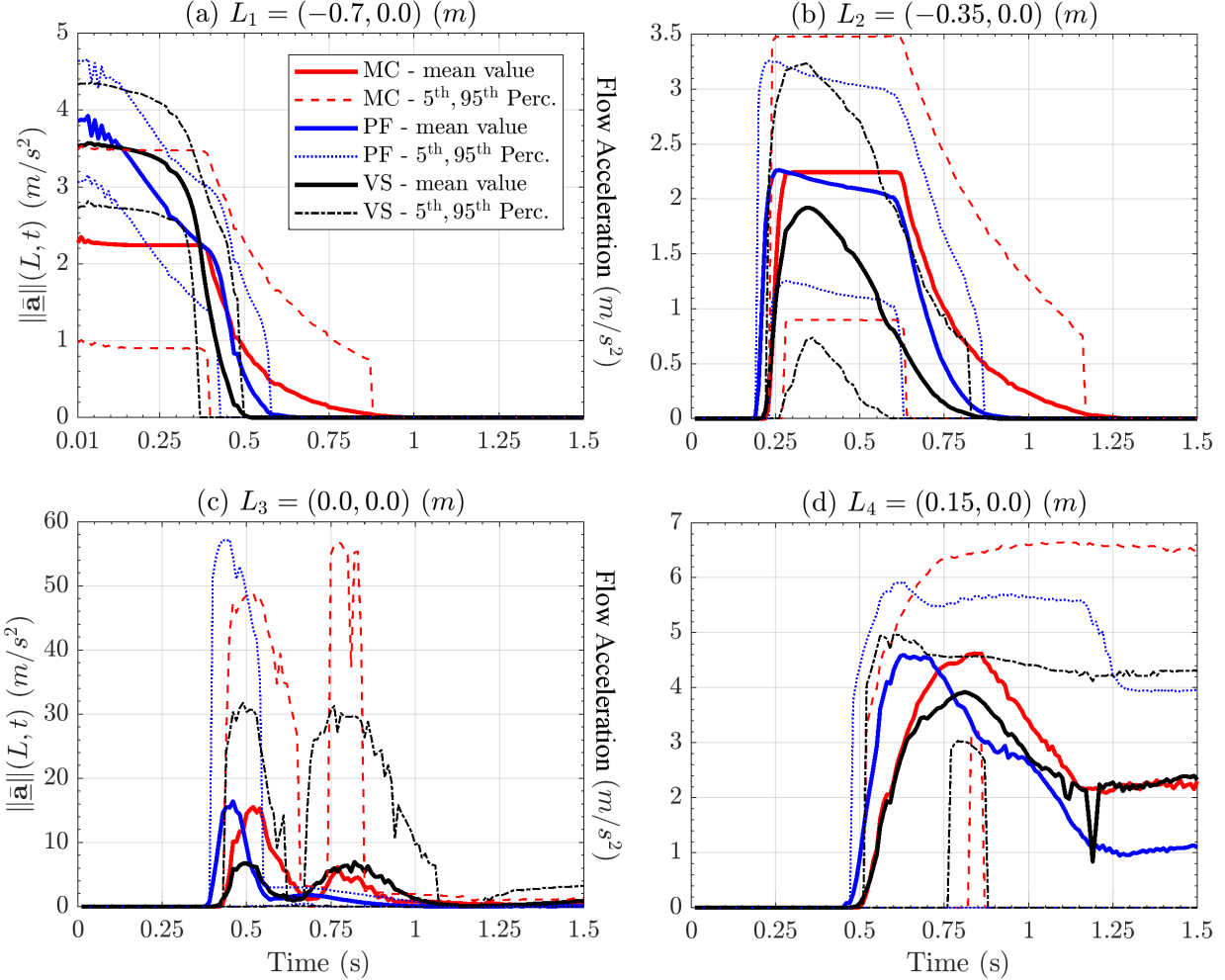


Figure 7: Records of flow acceleration magnitude (computed from LHS). Bold line is mean value, dashed lines are 5<sup>th</sup> and 95<sup>th</sup> percentile bounds. Different rheology models are displayed with different colors. Plots are at different scale.

Acceleration is the link between force terms and observable motion. We calculated it from the LHS of the dynamical equation, but using the RHS terms produces very similar results, although not identical due to the numerical approximations in solving the equations. In plot 7a, related to point  $L_1$ , MC and VS show a plateau before  $\sim 0.4$  sec, at  $\sim 2.5 \text{ m/s}^2$  and  $\sim 3.5 \text{ m/s}^2$ , respectively, while PF linearly decreases between those same values. In plot 7b, related to point  $L_2$ , are MC and PF to show a plateau, at  $\sim 2.2 \text{ m/s}^2$ , while VS has a more bell-shaped profile. UQ tells us that PF has a smaller uncertainty than the other models. In plot 7c, related to point  $L_3$ , all the models show a bimodal profile, with peaks at  $\sim 0.5$  sec and  $0.8$  sec. This is more accentuated in MC and VS, whereas the second peak is almost absent from PF's profile. The second peak is motivated by an increase of velocity in the down-slope direction after its reduction due to lateral spreading of material. At the first peak, acceleration values are significant, with average peaks in MC and PF both at  $\sim 15 \text{ m/s}^2$ , and 95<sup>th</sup> percentile plot reaching  $\sim 50 \text{ m/s}^2$  and  $\sim 55 \text{ m/s}^2$ , respectively. VS shows about halved acceleration peak values. At the second

peak, average acceleration values are similar in MC and VS, at  $\sim 5 \text{ m/s}^2$ . In contrast, 95<sup>th</sup> percentile plot is  $> 50 \text{ m/s}^2$  for MC, while  $\sim 30 \text{ m/s}^2$  in VS. In plot 7d, related to point  $L_4$ , the acceleration has a first peak at  $\sim 4 \text{ m/s}^2$ , and a final asymptote at  $\sim 2 \text{ m/s}^2$  for MC and VS,  $\sim 1 \text{ m/s}^2$  for PF. These values generally mean flow deceleration, and uncertainty is more relevant in MC and PF than in VS.

#### 4.1.3 Flow extents and spatial integrals

Figure 8 shows the spatial average of speed and Froude Number, in the three rheology models. Moreover, it shows the (maximum) lateral extent and inundated area of flow, as a function of time. Spatial averages and global quantities as maximum lateral extent and inundated area have smoother plots than local measurements. Most of the details observed in local measurements are not easy to discern.

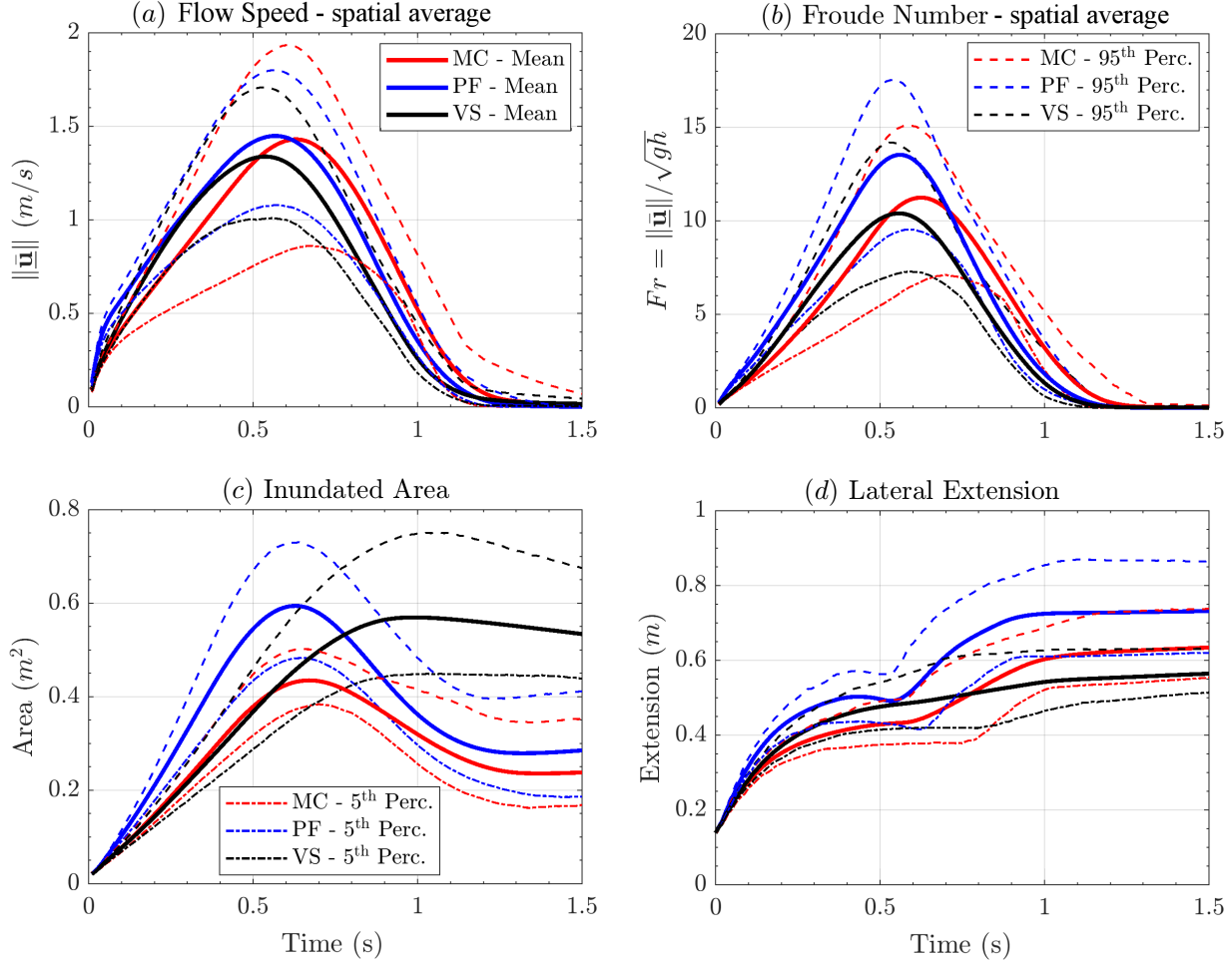


Figure 8: Comparison between spatial averages of (a) flow speed, and (b) Froude Number in addition to the flow (c) lateral extent, and (d) inundated area, as a function of time.

In plot 8a the speed shows a bell-shaped profile in all the models, with an average peak at  $\sim 1.4 \text{ m/s}$  and uncertainty range, given by 5<sup>th</sup> and 95<sup>th</sup> percentiles, of  $\pm 0.4 \text{ m/s}$  for PF and VS. VS is slightly slower, reaching  $\sim 1.3 \text{ m/s}$  in the average. MC shows a larger uncertainty range, of  $\pm 0.6 \text{ m/s}$ . The maximum speed is reached first by VS and PF at  $\sim 0.55 \text{ s}$ , and last by MC at  $\sim 0.65 \text{ s}$ . In plot 8b, also Froude Numbers have a bell-shaped profile. Fr peaks are temporally aligned with speed peaks, and are  $\sim 10$  in VS,  $\sim 11$  in MC,  $\sim 13.5$  in PF, on average. Uncertainty range is about  $\pm 4$  in all models. In plot 8c inundated area shows similar max values in PF and VS, at  $\sim 0.6 \text{ m}^2$  on average, and uncertainty of

$\pm 0.15m^2$ . MC is lower, at  $\sim 0.45m^2$  on average, and less uncertain,  $\pm 0.10m^2$ . VS does not decrease significantly after reaching the peak, whereas the other models contract their area, to approximately half of the maximum extent. In plot 8d the lateral extent starts equal to the pile diameter  $15cm$ , and then rises in two stages in MC and PF, the second and greater rise starting at  $\sim 0.6s$ , corresponding to the time of arrival at the change in slope  $L_3$  (see Fig. 6c). VS rises without showing two phases. After the first phase, average lateral extent is at  $\sim 50cm$  in PF and VS, while it is  $\sim 43cm$  in MC. Uncertainty range is  $\pm 7cm$  for all models at that time. Final extent is  $\sim 75cm$  in PF,  $\sim 65cm$  in MC,  $\sim 55cm$  in VS. Uncertainty range is  $\pm 5cm$  in VS, but rises to  $\pm 10cm$  in MC and PF.

## 4.2 Statistical analysis of dynamic quantities

In this section we focus on the force terms and related powers, as well as their statistical analysis. The decomposition of force terms follows the definitions in section 3.2. In particular, all the estimates assume a material density of the flow  $\rho = 805kg/m^3$ . This a fixed scaling factor, and the plots aspect is not affected by its value.

### 4.2.1 Power terms

Figure 9 shows the spatial integral of powers in the three rheology models. The spatial integration is performed on half spatial domain, due to the symmetry with respect to the flow central axis. Corresponding plots of the force terms are included in Supporting Information S2. The scalar product with velocity imposes a bell-shaped profile, as observed in Fig. 8a. In plot 9a the power of  $\mathbf{RHS}_1$  represents the effect of the gravity in all the models. It starts from zero and rises up to  $\sim 1.5W$  at  $\sim 0.55s$ , then decreases to zero after the material crosses the change in slope. Uncertainty range of  $\pm 0.5W$  on the peak values. MC decreases slower, and has a more significant uncertainty, after the change in slope. PF decreases faster. In plot 9b the power of  $\mathbf{RHS}_2$  represents the friction at the base of the flow. It is negative and peaks to  $\sim 1.1 \pm 0.2W$  in MC,  $\sim 1.0 \pm 0.2W$  PF,  $\sim 0.7 \pm 0.3W$  in VS. A similar bell-shaped profile is shared by the three models. In contrast, the force plots in Figure S2 show an initial ripple before  $\sim 0.1s$  and a plateau until  $\sim 1s$ . Basal friction power becomes negligible at the end, whereas the basal friction force in MC can be still significantly large. In plot 9c the power of  $\mathbf{RHS}_3$  is related to the curvature effects, and is not null only at the change in slope. It is always dissipative, i.e. opposing flow velocity, indeed it is equivalent to the friction due to the additional weight generated by centrifugal forces. It is weaker than  $-0.1W$  on average, ten times smaller than the previous powers, although MC lower percentile reaches  $\sim -0.25W$ . VS displays a bimodal profile, with a second and weaker peak at  $\sim 0.75s$ . In plot 9d the power of  $\mathbf{RHS}_4$  is related to the additional forces of the models, differently characterized. This term is really relevant in VS, although also in PF has a very short lasting positive peak up to  $0.3W$  before to become null at  $\sim 0.1s$ . This power in VS is a speed dependent term, always dissipative. It is bell shaped and null before  $\sim 0.1s$  and after  $\sim 1s$ . At the time of change in slope it is  $\sim -0.7W$ ,  $\pm 0.3W$ . In plot 9e the power of the total force  $\sum_{i=1}^4 \mathbf{RHS}_i$  summarizes the energy accumulation and dissipation, following a sinusoid profile. The profile is characterized by a positively valued stage before  $\sim 0.55s$  before the change in slope, and by a negatively valued stage after that, with bell-shaped profile, and a negative peak at  $\sim 0.75s$ . In the first stage MC increases more linearly, while PF and VS have a concave shape. In the second stage MC is affected by a larger uncertainty and the decrease occurs later in time of  $\sim 0.1s$ . PF and VS are remarkably similar, but VS wanes slightly faster.

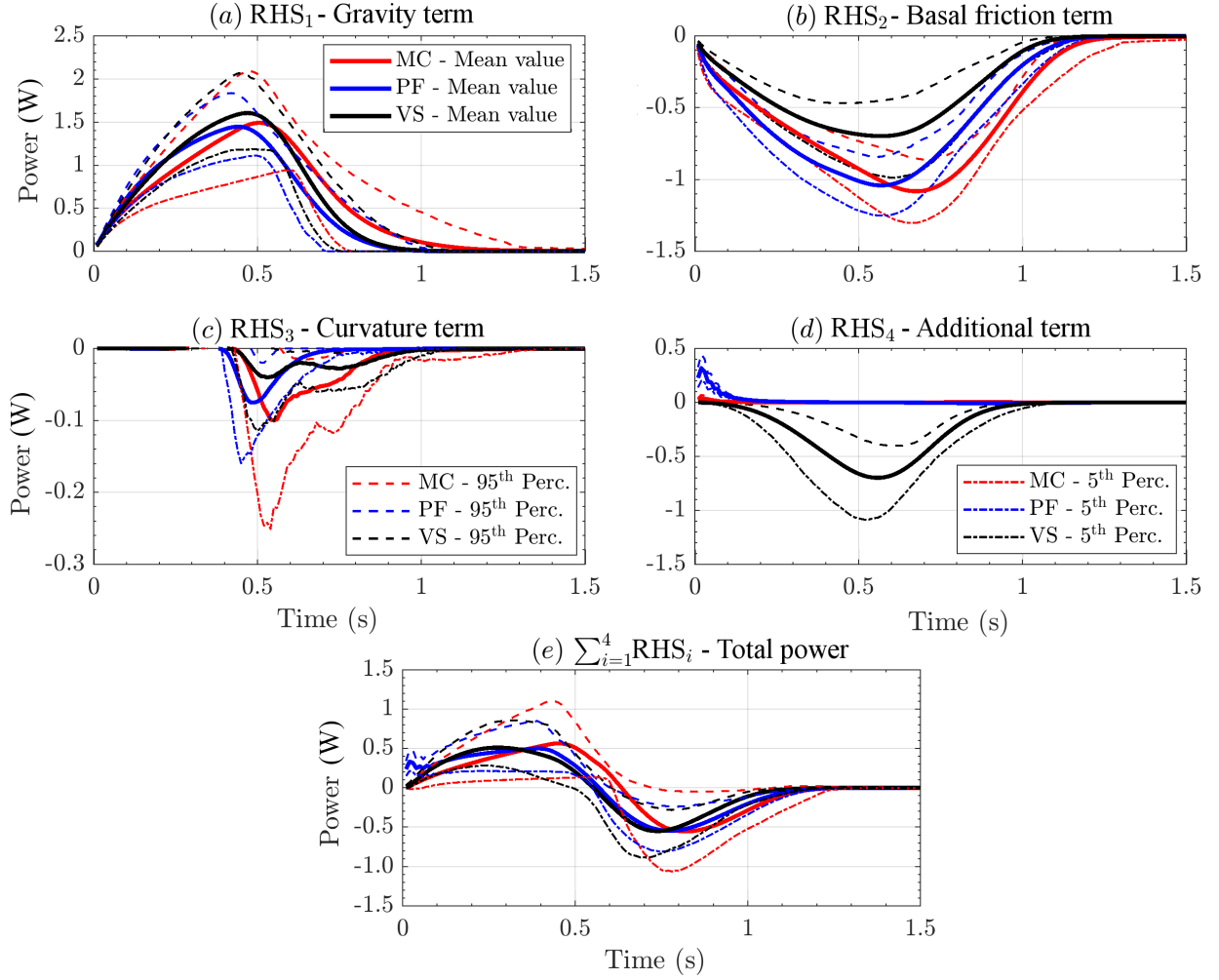


Figure 9: Spatial sum of the RHS powers. Bold line is mean value, dashed lines are 5<sup>th</sup> and 95<sup>th</sup> percentile bounds. Model comparison on the mean value is also displayed.

#### 4.2.2 Force dominance factors

Figure 10 shows the Dominance Factors ( $P_i$ ) $_{i=1,\dots,4}$  in the three rheology models, focusing on the RHS terms in the slope direction. A dominance factor is the probability of a force term to be the greatest one. Because these values are probabilities, they always belong to  $[0, 1]$ . The plots include also the probability of no-flow being observed at the considered point. The different models are plotted separately: 10a,d,g,j assume MC; 10b,e,h,k assume PF; 10c,f,i,l assume VS. The plots 10a,b,c are related to point  $L_1$ , placed on the initial pile. Only  $\mathbf{RHS}_1$  can be the dominant force, and no-flow probability is  $(1 - P_1)$ . Same thing in the plots 10d,e,f related to point  $L_2$ , placed in the middle of the slope. Then, plots 10g,h,i are related to point  $L_3$ , placed at the change in slope. In  $L_3$ ,  $\mathbf{RHS}_3$  can be the dominant term for a short time, with a peak probability of  $\sim 30\%$ . Plots 10j,k,l are related to point  $L_4$ , placed in the middle of the flat runout. In  $L_4$  only  $\mathbf{RHS}_2$  can be the dominant term, except in PF where there is  $\sim 10\%$  that  $\mathbf{RHS}_4$  is the dominant term at then ending-time.

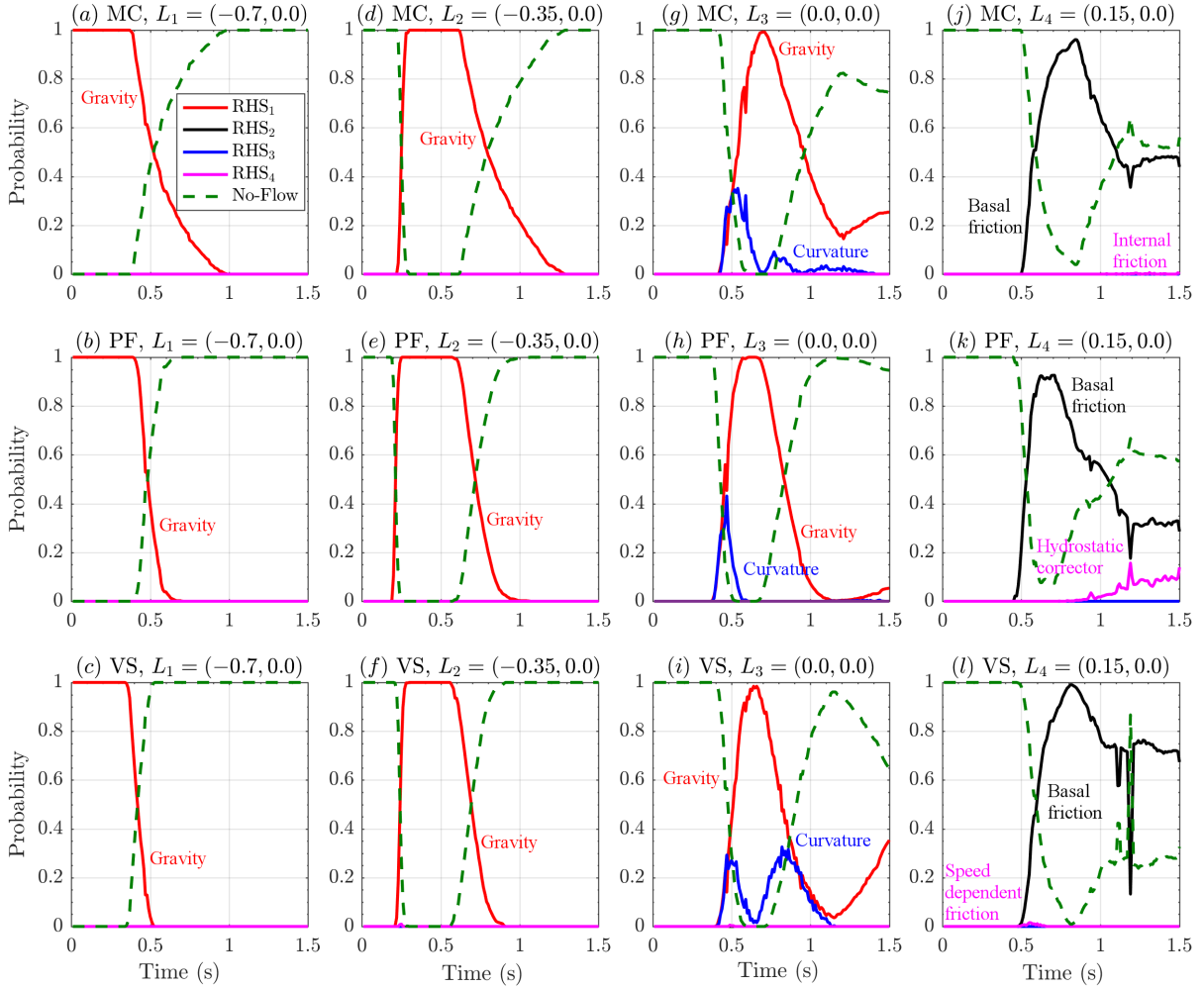


Figure 10: Records of dominance factors of **RHS** forces, in the slope direction, in four spatial locations of interest. Different rheology models are displayed with different colors. No-flow probability is also displayed with a green dashed line.

## 5 Results of large scale flows on the SW slope of Volcán de Colima (MX)

### 5.1 Flow height overview - Mohr-Coulomb model

In our second case study, the number of spatial locations is significantly higher than what previously assumed. We placed 51 points to span the entire inundated area, in search of different flow regimes, as displayed in Fig. 3. First we show the average flow height in all the locations, then, based on that, we select six points which we find representative of interesting flow regimes. Figure 11 assumes MC model, while the results related to PF and VS models are detailed on the six selected points.

Figure 11 shows the mean flow height,  $h(L, t)$ , at the 51 spatial locations of interest, according to MC.

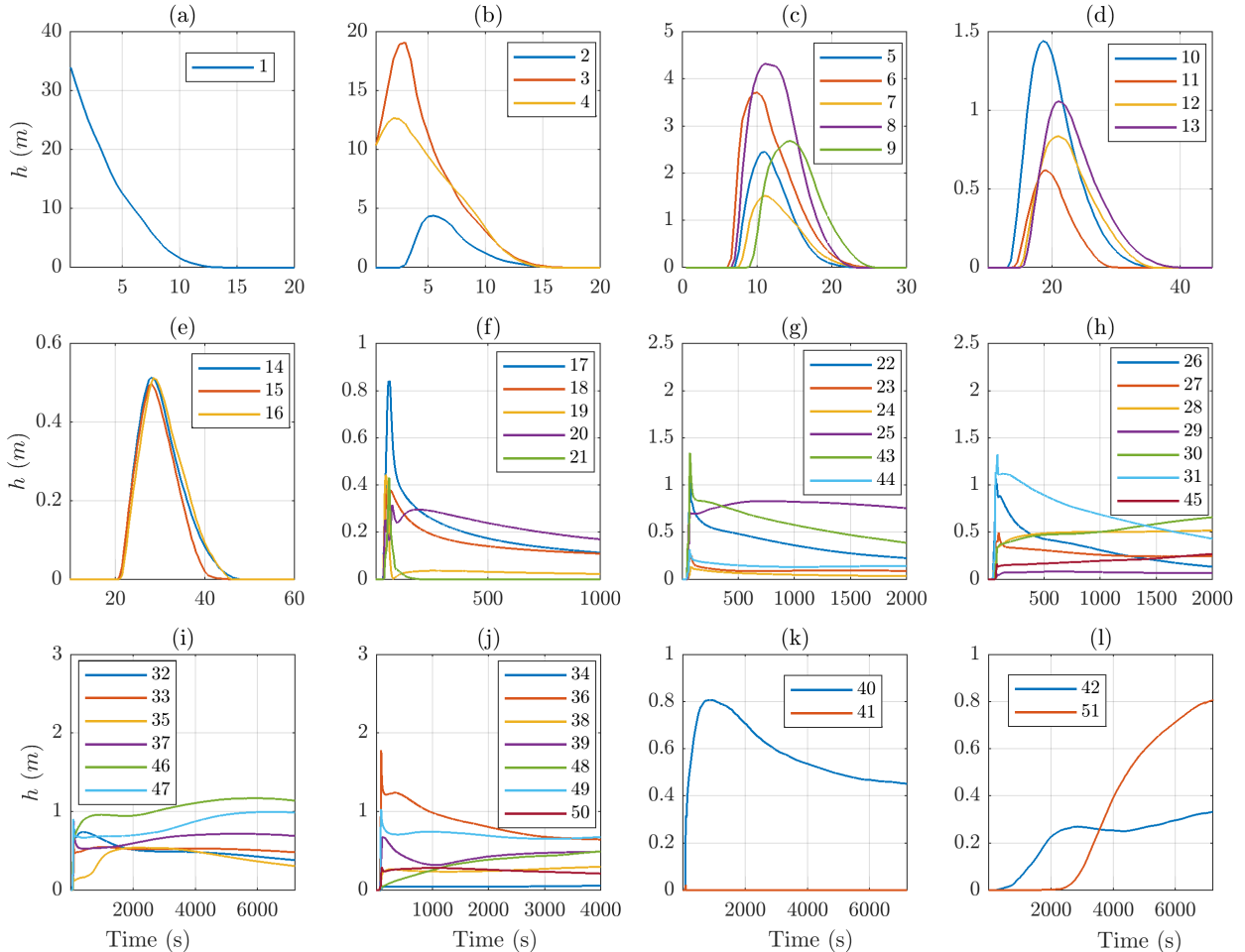


Figure 11: MC model, records of average flow height,  $h(L, t)$ , in 51 spatial locations of interest (Fig. 3).

Different plots have different scales on either time and space axes. In plot 11a, the only location is set on the center of the initial pile, and the profile is similar to what observed in point  $L_1$  of the inclined plane case study, in Fig.6a. In particular, the height decreases from the initial value to zero in  $\sim 15$ s. In plots 11b,c,d,e, the locations are set at less than  $\sim 1$  km radius from the initial pile (projected distance, without considering slope). Their profiles are similar to point  $L_2$  in Fig.6b. The height profile is bell-shaped, starting from zero and then waning back to zero in  $\sim 20$  s. All the dynamics occurs during the first minute. Plot (b) shows transitional features, and focuses on points at the boundary of

the initial pile. In plots 11f,g,h,i,j, points are set where the slope reduces, and the flow can channelize and leave a deposit. Projected distance from the initial pile is  $\sim 2 - 3$  km. The profiles are sometimes similar to  $L_3$  of Fig.6c, other times to  $L_4$  of Fig.6d, in a few cases showing intermediate aspects. In general is either observed an initial short-lasting bulge followed by a slow decrease lasting minutes and asymptotically tending to a positive height, or a steady increase of material height tending to a positive height. In both cases it is sometimes observed a bimodal profile in the first 5 minutes. Finally, plots 11k,l focus on three points set at about the runout distance of the flow, in the most important ravines, at  $\sim 4 - 5$  km projected distance from the initial pile. Profiles are similar to what observed in point  $L_4$  of Fig.6d. Plots of the Froude Number at the 51 points are included in Supporting Information S3 - strongly bimodal profiles and sharp changes are observed due to the interplay between flow height and flow speed.

## 5.2 Observable outputs - UQ on six selected locations

The six selected locations are  $[L_8, L_{10}, L_{17}, L_{39}, L_{43}, L_{46}]$ , displayed in Figure 12). First two points,  $L_8$  and  $L_{10}$  are both significantly close to the initiation pile. Points  $L_{17}$  and  $L_{43}$  are placed where the slope is reducing and the ravine channels start, and  $L_{39}$  and  $L_{46}$  are placed in the channels, further down-slope. Moreover,  $L_8$ ,  $L_{43}$ , and  $L_{46}$  are placed at the western side of the inundated area, whereas  $L_{10}$ ,  $L_{17}$ , and  $L_{39}$  are placed at the eastern side.

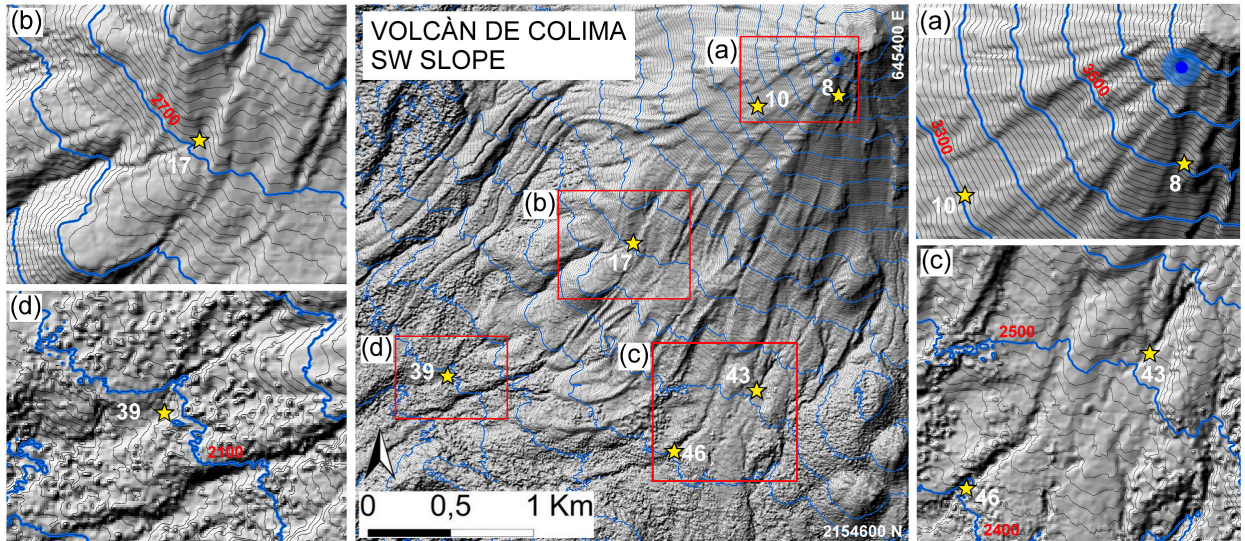


Figure 12: Volcán de Colima (Méjico) overview, including six selected sample sites (stars). In (a), (b), (c), (d) are enlarged the topographic features in proximity of those locations. Pile location is marked by a blue dot. Reported coordinates are in UTM zone 13N. Elevation isolines are included, at intervals of 10m in black, and 100m in bold blue. Elevation values in red.

Observable outputs include the flow height and acceleration as a function of time. In addition, flow area, and spatially averaged speed and  $Fr$  are displayed. Locally measured Froude Number is included in Supporting Information S4.

### 5.2.1 Flow height

Figure 13 shows the flow height,  $h(L, t)$ , at the points  $(L_i)_{i=8,10,17,39,43,46}$ , for the three rheology models. In plots 13a,b, we show the flow height in points  $L_8$  and  $L_{10}$ ,  $\sim 200m$  and  $\sim 500m$  from the initial pile, respectively.  $L_8$  is on the east side, and  $L_{10}$  on the west side of the flow. Models MC and PF display similar profiles, positive for less than 15s and bell-shaped. VS requires a significantly longer time to decrease, particularly in point  $L_{10}$ , where the average flow height is still positive after  $\sim 200s$ . Peak

average values in  $L_8$  are  $3.4m$  in  $PF$ ,  $4.3m$  in  $MC$ ,  $4.7m$  in  $VS$ . Uncertainty is  $\sim \pm 2m$ , halved on the lower side in  $MC$ , and  $PF$ . In  $L_{10}$ , models  $MC$  and  $PF$  are almost indistinguishable, with peak height at  $1.4m$  and uncertainty  $\pm 0.5m$ . Model  $VS$ , in contrast, has a maximum height of  $1.1m$  lasting for  $50s$ , and  $95^{th}$  percentile reaching  $3.7m$ . In plots 13c,e, we show the flow height in points  $L_{17}$  and  $L_{43}$ , both at  $\sim 2km$  from the initial pile, on the west and east side of the flow, respectively. All the three models show in both the points a fast spike during the first minute, followed by a slow decrease, still showing a positive average height after  $30$  minutes. Again,  $VS$  is significantly different from  $MC$  and  $PF$ , and has a secondary rise peaking at  $\sim 450s$ , which is not observed in the other models. This produces higher values for the most of the temporal duration, but converges to similar deposit thickness after more than  $1$  hour. Maximum values are  $1m$  for  $MC$ ,  $2m$  for  $PF$ , and  $1.5m$  for  $VS$ , in both locations. The  $5^{th}$  percentile is zero in all the models, meaning that the parameter range does not always allow the flow to reach those locations. The  $95^{th}$  percentile is always above  $5m$  in the models, except in  $VS$ , point  $L_{17}$ . In plots 13d,f, we show the flow height in points  $L_{39}$  and  $L_{46}$ , both placed at more than  $3km$  from the initial pile, on the west and east side of the flow, respectively. The three models all show an increasing profile, except in  $MC$ , in point  $L_{39}$ , which display an initial spike and a decrease before to rise again. A similar decreasing profile can be also observed in the  $95^{th}$  percentiles of all the models. It is significant that the  $5^{th}$  percentile of  $PF$  becomes positive after  $\sim 5400s$ , meaning that the flows almost surely have reached that location. Deposit thickness is  $\sim 0.5m$  in all the models in point  $L_{39}$ , and  $1.7m$  in  $VS$ ,  $1.6m$  in  $PF$ ,  $1.2m$  in  $MC$ , in  $L_{46}$ .

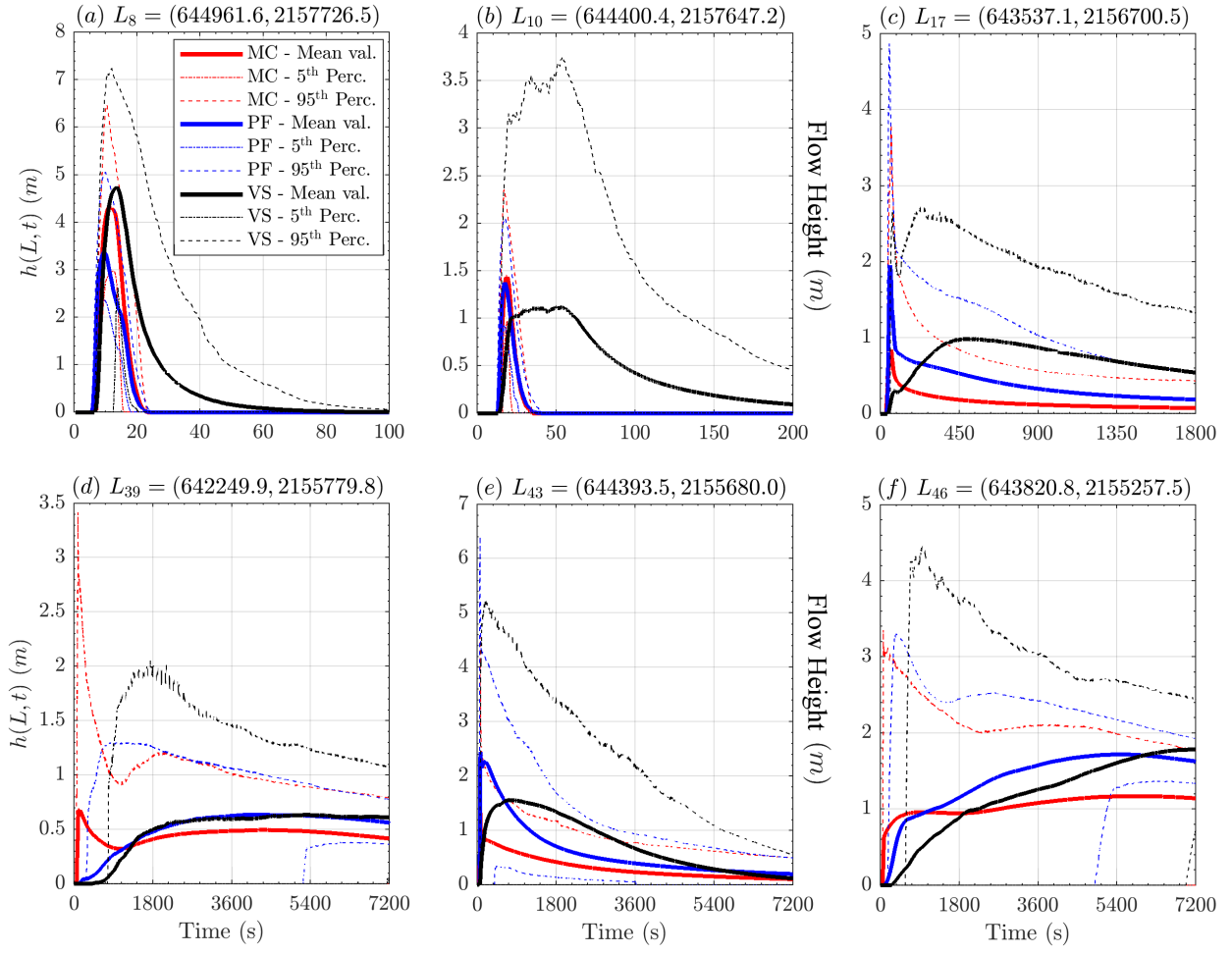


Figure 13: Records of flow height at six selected locations. Bold line is mean value, dashed/dotted lines are 5<sup>th</sup> and 95<sup>th</sup> percentile bounds. Different rheology models are displayed with different colors. Plots are at different scale, for simplifying lecture.

### 5.2.2 Flow acceleration

Figure 14 shows the flow acceleration,  $\|\bar{\mathbf{a}}\|(L, t)$ , at the points  $(L_i)_{i=8,10,17,39,43,46}$ , in the three rheology models.

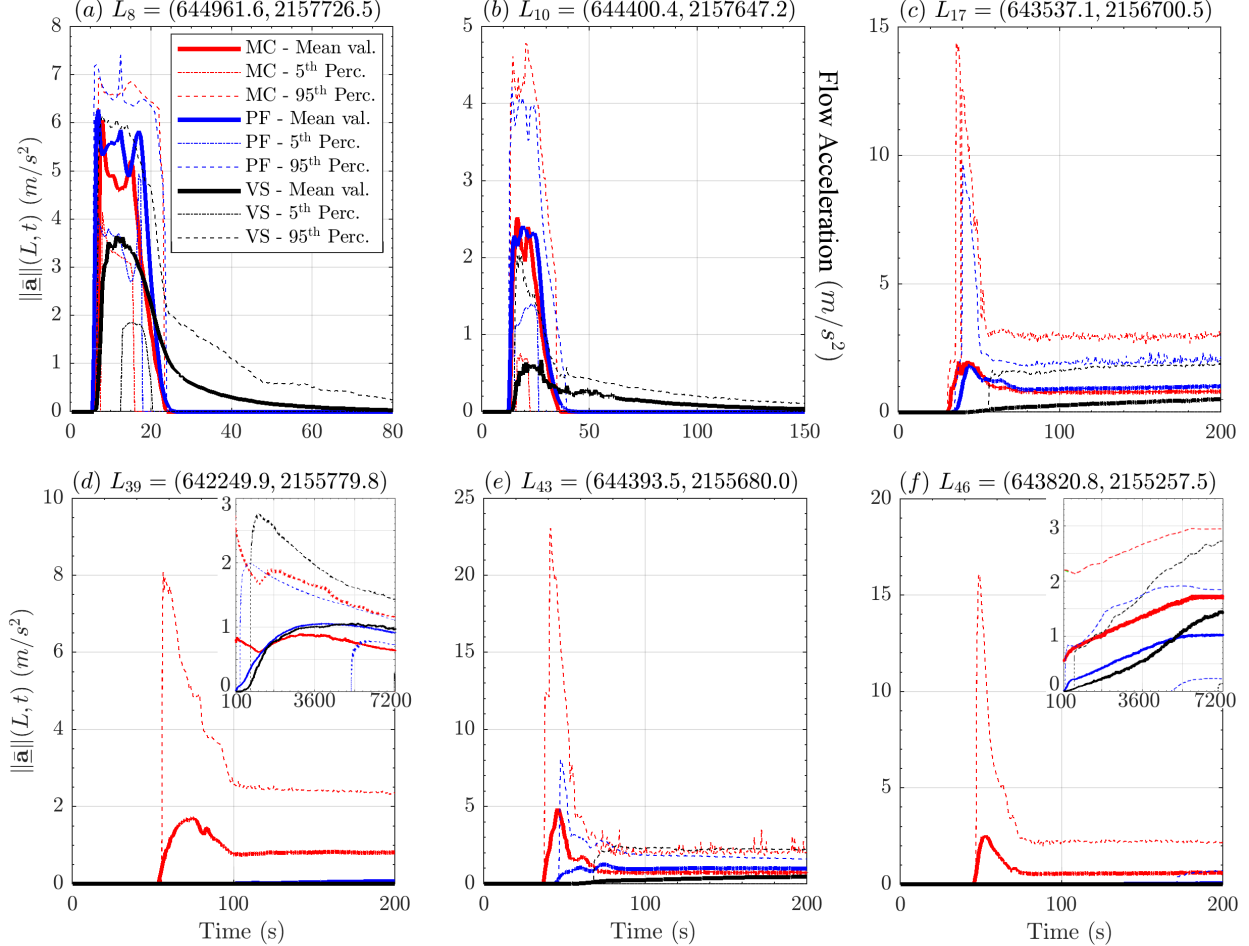


Figure 14: Records of flow acceleration magnitude (computed from LHS), in six selected locations. Records of points  $L_{39}$ ,  $L_{43}$ , and  $L_{46}$  are displayed at two different scales, according to the initial dynamics, in plots (d-f), and the asymptotic dynamics, in plots (g-i). Bold line is mean value, dashed lines are 5<sup>th</sup> and 95<sup>th</sup> percentile bounds. Different rheology models are displayed with different colors. Numerical noise affecting percentile curves in the small box of (f) has been averaged.

In plot 14a,b, MC and PF display a higher maximum acceleration, both at  $\sim 6m/s^2$  and  $\sim 2.5m/s^2$  in the first and second plot respectively, than VS,  $\sim 3.5m/s^2$  and  $\sim 0.5m/s^2$ , respectively. The latter has a slower decrease to zero. Uncertainty in VS is more significant in plot 14a, than in plot 14b. It is the opposite in MC and PF. In plot 14c, in MC and PF there can be a significant peak in acceleration, up to  $\sim 15m/s^2$  and  $\sim 10m/s^2$ , in the 95<sup>th</sup> percentile values, respectively. The same peak is absent in the average plots, which are significantly flat in all the models, displaying values at  $\sim 1m/s^2$  in MC and PF, and  $\sim 0.5m/s^2$  in VS, at  $\sim 200s$ . Plot 14e is similar, but PF is significantly reduced and lacks of the peak in the 95<sup>th</sup> percentile values. In plot 14d,f, only MC shows significant acceleration values. Plots 14g,h,i, are a zoom on the acceleration values in the distal locations, displayed on a long time window of 7200s. The last two plots are more noisy, but possess an increasing trend. All the three show, in all the models, values up to  $\sim 1m/s^2$ . In general, PF acceleration tends to be lower than in the other models.

### 5.2.3 Flow area and spatial integrals

Figure 15 shows the spatial average of speed and Froude Number, in the three rheology models. Moreover, it shows the inundated area of flow, as a function of time.

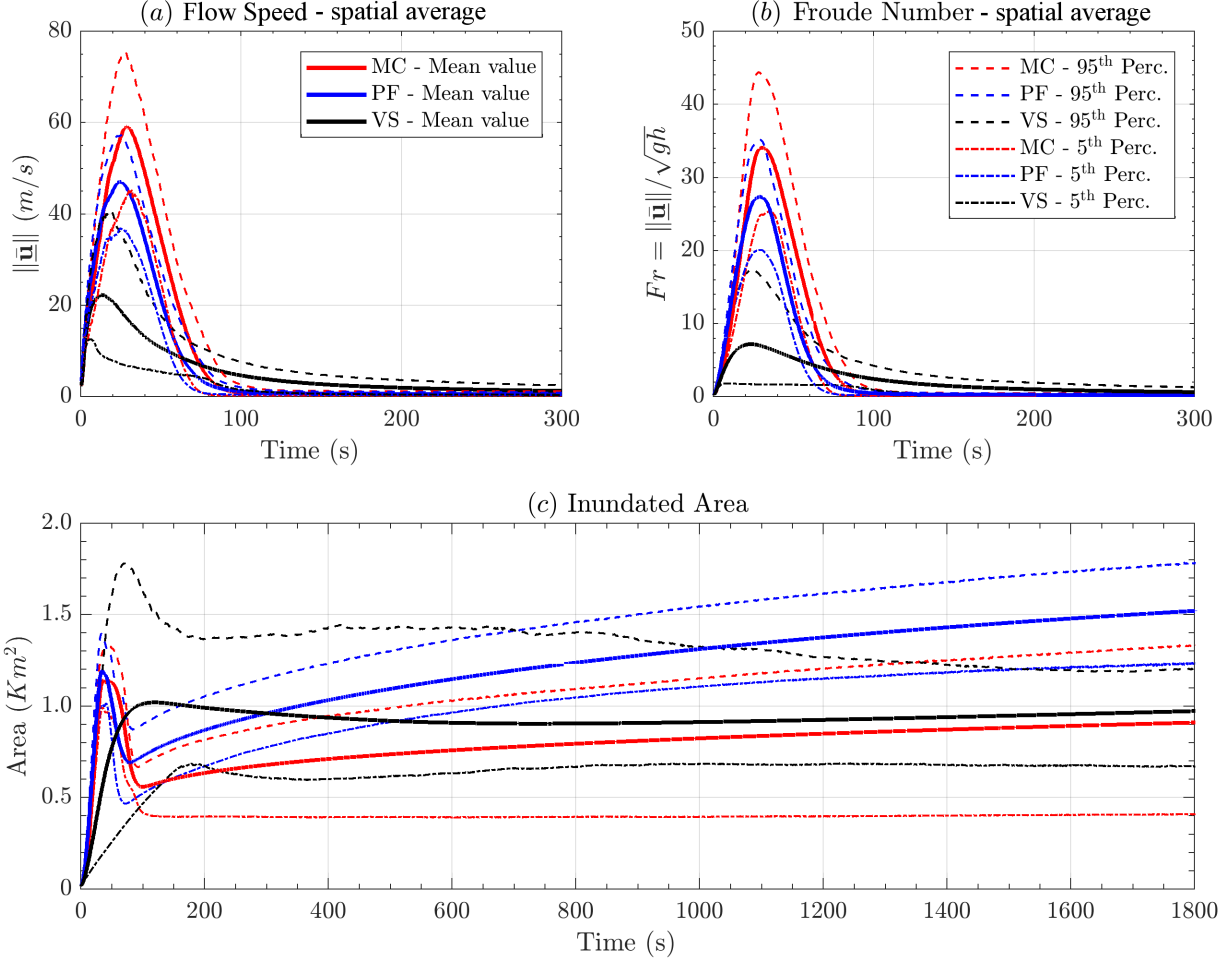


Figure 15: Comparison between spatial averages of (a) flow speed, and (b) Froude Number, in addition to the (c) inundated area, as a function of time.

Like in Fig.8, spatial averages and inundated area have smoother plots than local measurements, and most of the details observed in local measurements are not easy to discern. In plot 15a the speed shows a bell-shaped profile in all the models, but whereas the values were significantly similar in the inclined plane experiment, in this case the maximum speed is  $\sim 60m/s$  in MC,  $\sim 50m/s$  in PF,  $\sim 20m/s$  in VS, on average. Uncertainty is  $\pm 18m/s$  in MC, similar, but skewed on the larger values in VS,  $\pm 10m/s$  in PF. In plot 15b, the Froude profile is very similar to the speed, but the difference between VS and the other models is accentuated. Maximum values are  $\sim 50$  in MC,  $\sim 38$  in PF,  $\sim 5$  in VS, whereas uncertainty is  $\pm 10$  in MC,  $\pm 7$  in PF, and skewed  $[-5, +10]$  in VS. In plot 15c, inundated area has a first peak in MC and PF, both at  $\sim 1.15km^2$ , followed by a decrease to  $0.55km^2$  and  $0.7km^2$ , respectively, and then a slower increase up to a flat plateau at  $0.9km^2$  and  $1.5km^2$ , respectively. Uncertainty is  $\sim \pm 0.2km^2$  in both MC and PF until  $\sim 100s$ , and then it increases at  $\pm 0.3km^2$  and  $[-0.5, +0.4]km^2$ , respectively. In MC the increase of uncertainty is concentrated at  $\sim 100s$ , while it is more gradual in PF. VS has a different profile. The initial peak is significant only in the 95<sup>th</sup> percentile values, and occurs significantly later, i.e. at  $\sim 100s$  against  $\sim 50s$  in MC and PF. It is of  $\sim 1km^2$  on the average, but up to  $\sim 1.8km^2$ .

in the 95<sup>th</sup> percentile. The decrease after the peak is very slow and the average inundated area is never below  $0.85\text{km}^2$ , and eventually reaches back to  $\sim 1\text{km}^2$ . Uncertainty is  $[-0.3, +0.2]\text{km}^2$ .

### 5.3 Statistical analysis of dynamic quantities

All the estimates in this section assume the material density of the flow  $\rho = 1800\text{kg/m}^3$ . This a fixed scaling factor, and the plots aspect is not affected by its value.

#### 5.3.1 Power terms

Figure 16 shows the spatial sum of the powers, for the three rheology models. Corresponding plots of the force terms are included in Supporting Information S5.

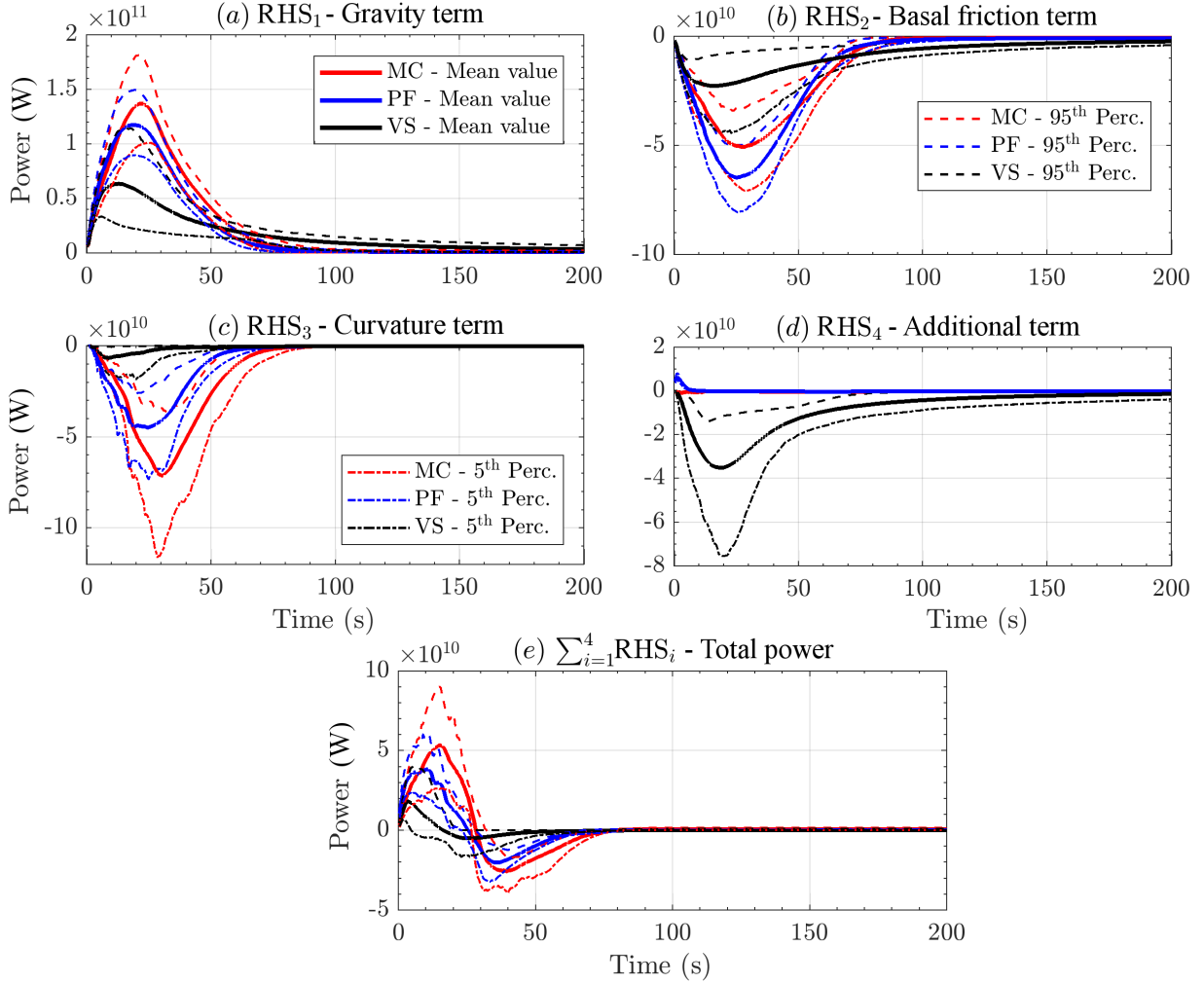


Figure 16: Spatial sum of the RHS powers. Bold line is mean value, dashed lines are 5<sup>th</sup> and 95<sup>th</sup> percentile bounds. Model comparison on the mean value is also displayed.

The scalar product with velocity imposes the bell-shaped profile already observed in Fig. 9a. In plot 16a the power of  $\text{RHS}_1$  represents the effect of the gravity in all the models. It starts from zero and rises up to  $\sim 1.4\text{e}11\text{W}$  in MC,  $\sim 1.2\text{e}11\text{W}$  in PF,  $\sim 6.5\text{e}10\text{W}$  in VS. Uncertainty is  $\pm 4\text{e}10\text{W}$  in MC,  $\pm 3\text{e}10\text{W}$  in PF,  $[-4\text{e}10, +5\text{e}10]\text{W}$  in VS. The decrease of gravitational forces is related to the slope reduction, and

this decrease is more gradual in VS than in the other models. In Figure S5, at  $\sim 10s$  the forces in all the models show a slowing down of the decrease, which is permanent in VS, and lasting  $\sim 10s$  in MC and PF. This is not visible in the power plots. In plot 16b the power of  $\mathbf{RHS}_2$  represents the effect of the basal friction in all the models. It is negative and peaks to  $\sim -6.5e10W$  in MC,  $\sim -5e10W$  in PF,  $\sim -2e10W$  in VS. In VS this dissipative power is significantly more flat than in the other models. MC and PF show negligible powers after  $\sim 100s$ , VS after  $\sim 200s$ . Uncertainty is  $\pm 2e10W$  in MC,  $\pm 1.5e10W$  in PF,  $[-2e10, +1e10]W$  in VS. In Figure S2, the basal friction force in MC shows a bimodal profile with a peak at  $\sim 5s$  and a second one at  $\sim 60s$ . This is not visible in powers. In PF, the plot starts from stronger values than in the other models, but it is also the faster to wane. In plot 16c the power of  $\mathbf{RHS}_3$  represents the effect of the curvature of terrain. It has a similar profile to the corresponding force, peaking to  $\sim -7e10W$  in MC,  $\sim -4.5e10W$  in PF,  $\sim 5e9W$  in VS. The rise of this dissipative power has a similar profile, but a different duration between the models. The decrease is more gradual in VS. Uncertainty on the peak value is  $[-4.5e10, +3.5e10]W$  in MC,  $[-2.5e10, +2e10]W$  in PF,  $[-1e10, +5e9]W$  in VS. The three models all show a bell-shaped profile, MC and PF waning to zero at  $90s$ , VS at  $\sim 30s$ . In plot 16d the power of  $\mathbf{RHS}_4$  has a different meaning in the three models. In MC it is the internal friction term, and it only has almost negligible ripple visible in the first second. In PF it is a depth averaged correction in the hydrostatic pressure, and has an almost negligible effect only during the first second of simulation, at  $5e9W$ . It becomes null at  $\sim 10s$ . In VS, instead, it is a speed dependent term, and has a very relevant effect. The plot shows a bell-shaped profile, with a peak of  $\sim -3.5e10W$ ,  $[-2e10, +1e10]W$ . After that, this dissipative power gradually decreases, and becomes negligible at  $200s$ . In plot 16e the power of the total force  $\sum_{i=1}^4 \mathbf{RHS}_i$  summarizes the energy accumulation and dissipation, following, like in the inclined plane case study, a sinusoid profile. First is observed a steep increase due to the domination of the gravity upon the friction, then a negative part when the friction stops the dynamics. As displayed in Fig. 9e, MC profile is delayed compared to the others, and is affected by a larger uncertainty.

### 5.3.2 Force dominance factors

Figure 17 shows the Dominance Factors  $(P_i)_{i=1,\dots,4}$ , in the three rheology models and focusing on the RHS terms moduli, in the three selected points  $L_8$ ,  $L_{10}$ , and  $L_{17}$ , closer than 1 km to the initial pile (in horizontal projection).

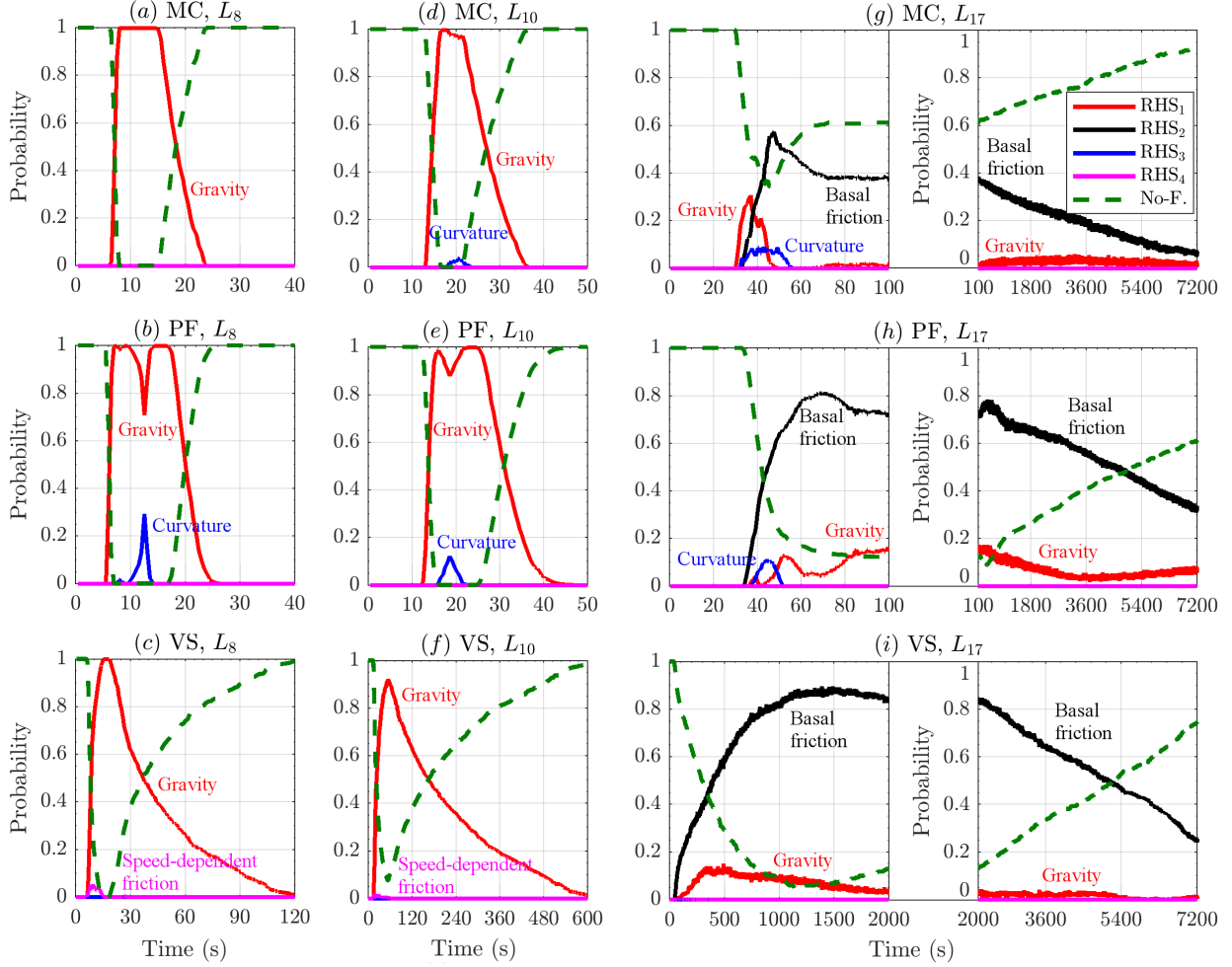


Figure 17: Records of dominance probabilities of **RHS** force moduli, at three spatial locations of interest, in the first km of runout. Bold line is mean value, dashed/dotted lines are 5<sup>th</sup> and 95<sup>th</sup> percentile bounds. Different rheology models are displayed with different colors. No-flow probability is also displayed.

The plots 17a,b,c and 17d,e,f are related to point \$L\_8\$ and \$L\_{10}\$, respectively. They are significantly similar. **RHS<sub>1</sub>** is the dominant force with a very high chance, \$P\_1 > 90\%\$. In MC and PF it is observed a small chance, i.e. \$P\_3 = 5\% - 30\%\$ at most, of **RHS<sub>3</sub>** being the dominant force for a short amount of time, i.e. \$\sim 5s\$. This occurs in the middle of the time interval in which the flow is almost surely inundating the points, and no-flow probability is negligible. In VS it is observed a \$P\_4 = 5\%\$ chance of **RHS<sub>4</sub>** being dominant, for a few seconds, anticipating the minimum of no-flow probability. Plots 17g,h,i, are related to point \$L\_{17}\$, and the plots are split in two sub-frames, following different temporal scales. In all the models, **RHS<sub>2</sub>** is the most probable dominant force, and its dominance factor has a bell-shaped profile, similar to the complementary of no-flow probability. In all the models, **RHS<sub>1</sub>** has a small chance of being the dominant force. In MC, this is more significant, at most \$P\_1 = 30\%\$, for \$\sim 20s\$ after the flow arrival, and has again about \$P\_1 = 2\%\$ chance to be dominant in [100, 7200]s. In PF, the chance is \$P\_1 = 15\%\$ at most, and has two maxima, one short lasting at about 55s, and the second in [100, 500]s. Also in VS, the chance is at most \$P\_1 = 15\%\$, reached at [300, 500]s, but its profile is unimodal in time, and becomes lower than \$P\_1 = 2\%\$ after 2000s. In MC and PF, **RHS<sub>3</sub>** has a chance of \$P\_3 = 10\%\$ of being the dominant force, for a short amount of time [30, 50]s and [40, 50]s, respectively.

Figure 18 shows the Dominance Factors \$(P\_i)\_{i=1,\dots,4}\$, in the three rheology models, in the three selected points \$L\_{39}\$, \$L\_{43}\$, and \$L\_{46}\$, over 2 km far away from the initial pile.

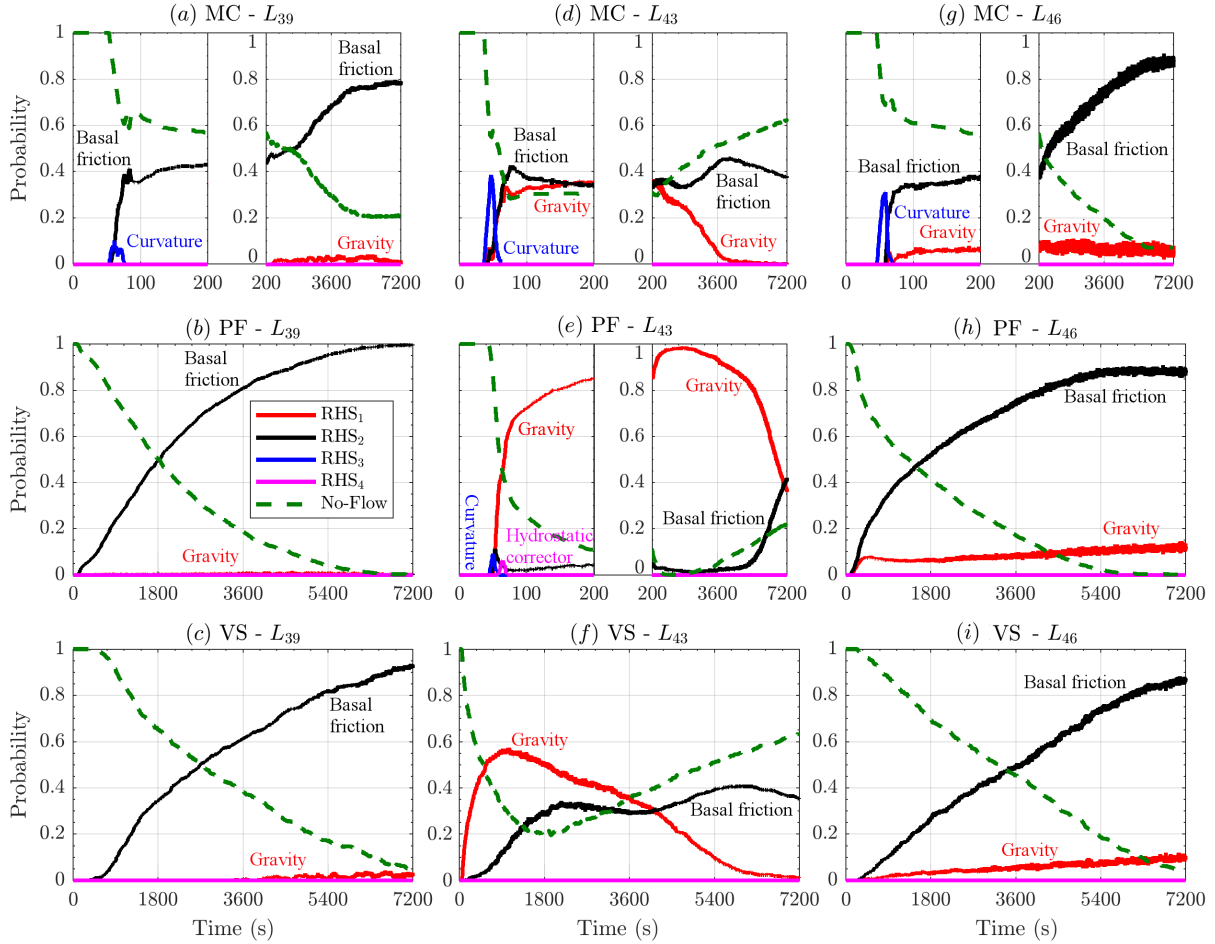


Figure 18: Records of dominance probabilities of **RHS** force moduli, at three spatial locations of interest, after 2 km of runout. Bold line is mean value, dashed/dotted lines are 5<sup>th</sup> and 95<sup>th</sup> percentile bounds. Different rheology models are displayed with different colors. No-flow probability is also displayed.

The plots 18a,b,c and 18g,h,i are related to point  $L_{39}$  and  $L_{46}$ , respectively, and they are significantly similar. Those points are both in the most distal part of the ravines, on the western and eastern side of the inundated area, respectively. They are also similar to the dominance factors at point  $L_{17}$ , shown in plots 17g,h,i, but the no-flow probability never becomes negligible in this case. The probability of **RHS<sub>2</sub>** being the dominant force is  $P_2 > 90\%$  till the end of the temporal window. Moreover, **RHS<sub>1</sub>** does not show any initial peak in  $P_2$ , and generally increases slowly, reaching at most  $P_2 = 10\%$  chance of being the dominant force in  $L_{46}$ , after more than 3600s, in all the models. Plots 18d,e,f, are related to point  $L_{43}$ , are remarkably different. In MC, either **RHS<sub>1</sub>** and **RHS<sub>2</sub>** can be dominant forces, both with chances of  $\sim 35\%$  in the first 200s. Then, **RHS<sub>2</sub>** increases its chance, and becomes the only dominant force after 3600s. The no-flow probability is never below 30%. **RHS<sub>3</sub>** has a chance  $P_3$  up to 35% for a short amount of time, i.e. [40, 60]s. In PF, **RHS<sub>1</sub>** is the dominant force with chance above  $P_1 = 90\%$  until 3600s. **RHS<sub>2</sub>** chance rises only in the very last amount of time, reaching  $P_2 = 40\%$  at 7200s, at the same level of  $P_1$ . The no-flow probability is very low during the most of the temporal window, rising at 20% only at 7200s. Both **RHS<sub>3</sub>** and **RHS<sub>4</sub>** have a short peak of dominance factor, at about 10% for a few seconds, at [50, 60]s. Finally, in VS the no-flow probability is never below 20%, and the profile is similar to MC, although **RHS<sub>1</sub>** is more relevant, up to 4000s. The other force are almost never dominant.

## 6 Discussion on the comparative anatomy of geophysical flow models

In this section we summarize the general features which differ between the models, with the purpose of depicting a thorough identikit of them, and breaking down the effects of the modeling assumptions listed in section 2.3. The main focus is on the average plots, but the uncertainty percentiles are also considered, and often they exalt the differences between the models.

### 6.1 Characteristic features and their motivations

Even in the process of the preliminary alignment of the parameter ranges, the differences features in the models already affected the shape of the inundated area, both in the small flow on the inclined plane, and in the large scale geophysical flow. In Fig. 4 the max runouts display a larger lateral extent in PF, and a bent shape in VS where the lateral wings remain behind the central section of the flow. In Fig. 5, the three models look clearly different both in the min-runout and in the max-runout cases. Even if the maximum runout is matched, MC displays a further distal spread before entering the ravines, PF shows a larger angle of lateral spread at the initiation pile, VS is less laterally extended and generally looks significantly channelized, and displays several not-inundated spots due to minor topographical coulées.

#### 6.1.1 Flow height

Flow height gives additional insight on the model features. In Fig. 6, MC looks more distally stretched, but starts to deposit material earlier and closer to the initial pile. PF height is generally shorter, and displays a small temporal anticipation in its arrival at the sample points. These features are probably due to the hydrostatic correction term, which pushes forward the material at the very beginning, during the pile collapse. Also, the interpolation between the minimum  $\phi_1$  and maximum  $\phi_2$  friction angles, as a function of flow height and speed, plays a role in the linear cut in the flow height profile when the flow thins on the slope. VS tends to be higher than the other models, because of the reduced lateral spreading of material. In Fig. 13 the large scale flow height plots allow us to classify the points according to their similarity with the four points of the small scale flow. There is a significant feature which was not observed in the small scale flow - VS is temporally stretched, and material arrives later and stays longer in the sample points. This is clearly a consequence of the speed dependent term.

#### 6.1.2 Flow acceleration

Flow acceleration brings our analysis from the mechanics to the dynamics of the flow. In Fig. 7, at the point  $L_2$  on the slope, MC has a flat plateau, while PF is linearly decreasing, and VS is bell shaped. Those differences are a consequence of the assumptions behind the models - double angle in PF, and speed dependent term in VS. At the slope change point  $L_3$ , VS and MC display a bimodal profile in the acceleration. This is not a statistical effect, but it is physically observed in single simulations. The first maximum is when the head of the flow hitting the ground, while the second maximum is when the accumulating material in the tail arrives. In VS the maxima are equal, because its tail is not laterally spread and hits the ground compactly. In contrast, PF does not show such a second peak, due to the accentuated lateral spreading in the tail. In point  $L_4$  on the flat runway, the average acceleration in PF is lower than in the other models at the end of the simulation time, probably because the material stops more suddenly, and the probability of no deposit is greater. In Fig. 14 VS decreases faster, but also displays a fatter tail in the acceleration. MC reaches the most distal sample points earlier and with a more significant acceleration.

#### 6.1.3 Flow extents and spatial integral

In Fig. 8 the average speed and Froude Number of the different models are significantly similar, and this points to the fact that the differing features are mostly localized in space. VS is confirmed to be significantly slower than the other models, after the initial collapse. Moreover, it is the only model which presents a significant amount of long lasting and slowly moving material. Inundated area in PF has a greater maximum value, because of the accentuated lateral spread. In VS the inundated area almost does

not decrease from its peak, because of the strictly increasing lateral spread. Vice versa, lateral spread in MC and PF has a temporary stop when the bulk of the flow hits the ground. This is a consequence of the interplay of accumulating material and the push of new material, which is stronger in the middle than in the lateral wings. In PF lateral extent is even decreasing slightly for a short time. The hydrostatic correction term may generate the pull reducing the lateral extent. In Fig. 15 average speed and Froude Number display that VS slower speed is not a local feature. Inundated area is again significantly larger in PF.

#### 6.1.4 Power and force terms

Power terms have several features in common with the corresponding forces, and provide the decomposition of the acceleration sources. Main dissimilarity between forces and powers is that gravitational and basal friction powers have a profile starting from zero when the flow initiates, because the flow speed starts from zero. In Fig. 9 the difference between models is particularly relevant in term  $\mathbf{RHS}_4$ . Speed dependent power in VS is at least one order of magnitude larger than the maximum values of the corresponding terms in MC and PF. Those are decreasing to zero after a short time from the initiation. Hydrostatic correction in PF is clearly positive in the speed direction, and hence contributing to push the flow ahead, at the beginning. The effects of internal friction in MC are almost negligible, and initially positive, then negative. This is motivated by an initial compression of the material during the pile collapse, followed by its stretching. It is worth remarking that  $\mathbf{RHS}_2$  and  $\mathbf{RHS}_3$  are both smaller in VS, due to the lower basal friction angles involved. In Fig. 16, the differences are accentuated, because of the topography complexity. Gravity term is larger in VS, because a portion of the flow lingers on the higher slopes for a long time. Basal friction has a higher peak in PF, due to the effect of the interpolation of the friction angle to the larger value  $\phi_2$  in several portions of the flow.

#### 6.1.5 Force dominance factors

The force dominance factors illustrate the predominant force term through time and the probability of no-flow. In Fig. 10 the differences between the models are minor in the inclined plane case study. In general, there is only a single dominant force, and its profile is complementary with the no-flow probability. More details can be found in the force contributions analysis (Appendix B and Supporting Information S6 and S7). Only in the slope change point  $L_3$  the differences are remarkable. Curvature term dominance probability is bimodal in MC and VS, and in MC the second peak is smaller. The profile is similar to the spatial average of the force term. In the flat runway, at point  $L_4$ , in PF the hydrostatic correction can be the dominant force with a small chance. In Fig. 17 and 18, the complexity in the dominance factors is greater. At the points  $L_8$  and  $L_{10}$ , proximal to the initiation, gravitational force is dominant with a high probability until the no-flow probability become predominant. Curvature force can be dominant in MC and PF, when the no-flow change is zero, and for a short time. Gravitational force is dominant for a much larger time, because of the longer presence of the flow. The speed dependent friction can be dominant with a small probability, at the beginning of the dynamics, when flow is faster. At the points  $L_{17}$ ,  $L_{39}$ , and  $L_{46}$ , the basal friction is dominant with high probability.  $L_{17}$  is left by the flow, whereas  $L_{39}$ , and  $L_{46}$  have a deposit at the end with a high chance. In general, in MC the no-flow probability tends to be larger than in the other models, because part of the parameter spaces stops earlier, or completely leaves the site. Again, curvature can have a small chance to be dominant in MC and PF, particularly when the speed is high. Point  $L_{43}$  is particularly interesting. It is not close to the initiation, but it is placed right after a local hill. This location shows an intermediate regime between the proximal points and the distal ones. The no-flow probability is increasing at the end, meaning that the material is leaving the site, like in  $L_{17}$ . Moreover, the gravity can be dominant like in the proximal points, but also the bed friction can be dominant, and in MC and VS both the two forces have similar chances to be dominant for the most of the time of the simulation. In PF, only the gravitational force is dominant with a high chance, and the no-flow probability is almost null, meaning that there is accelerating material for the most of time. This is probably because point  $L_{43}$  is placed in a place right downhill of a place where a significant amount of material stops according to that model.

## 7 Conclusions

This study presents a new statistical procedure for the comparative analysis of different models for the rheology of geophysical mass flows. The method enabled us to break down the effects of the different physical assumptions in the dynamics, providing an improved understanding of what characterizes each model. We considered a Monte Carlo simulation on a range of parameter inputs, and estimated the mean and the uncertainty range of the corresponding outputs. Fitting the results on a specific flow was thus not necessary, and the procedure unfolded the physics of the models in a general framework. We also developed the concept of force dominance factor, in the study of the force terms in the different regions of space and time. This paves the way to future research aimed at designing a new generation of algorithms, which could completely bypass the search for a unique best model. They would go beyond the concept of alternative models, first decomposing them into their characterizing features, and then focusing instead on a more flexible selection of the assumptions which are locally suitable for each specific part of the simulation.

In particular, we presented:

- a short review of the assumptions characterizing three commonly used rheologies of Mohr-Coulomb, Poliquenne-Forsterre, Voellmy-Salm. This included a qualitative list of such assumptions, and the breaking down of the different terms in the differential equations.
- a preliminary procedure for selecting the portions of the parameter ranges of the models which produced consistent outputs. This was fundamental because the model comparison cannot focus on the modeling differences if the scales of the stress tensor were on different scales.
- an articulated statistical framework, processing the mean, and the uncertainty range of many mechanical and dynamical quantities in the flow simulation. A new function was featured in the TITAN2D solver, capable of producing local measurements of those quantities at selected sites. Spatial integrals and spatial averages were also performed, illustrating the characteristics of the entire flow under the different models. The new concept of force dominance factors enabled a simplified description of the local dynamics.
- the detailed results of the procedure applied to two different case studies: an inclined plane with a flat runway, and the real DEM on the SW lobe of Volcán de Colima (MX). All the differences were quantitatively commented.
- a final discussion, explaining all the observed features in the results on the light of the known physical assumptions of the models, and the evolving flow regime in space and time.

Our statistical analysis based on UQ depicted three very different models, due to the different assumptions underlying to them. Compared to a classical MC model, PF lacks of internal friction and this produces an accentuated lateral spread. This is increased by the hydrostatic correction, which briefly pushes the flow ahead and laterally during the initial collapse. That force can also have some minor effects in the final deposit accumulation. The interpolation of the smaller bed friction angle  $\phi_1$  with the larger value  $\phi_2$ , suddenly stops the flow if it thins compared to its speed. This mechanism does not allow for large speed peaks. Instead in VS, the speed dependent friction has a great effect in reducing lateral spread and producing channeling features even due to minor ridges in topography. The flow tends to be significantly slower and more stretched in the slope direction. The effects of the different formulation of the curvature term are less impacting than the effects of the lower basal friction and speed.

The procedure may be applied to other models, or modeling assumptions. Moreover, the two case studies considered had the purpose of exploring two very different scale of flows, the first on a controlled setting, the second on a real topography. Additional research concerning other case studies, and different parameter ranges, might reveal other flow regimes, and hence differences in the consequences of the modeling assumptions under new circumstances.

## 8 Appendix A: Latin Hypercubes and orthogonal arrays

The Latin Hypercube Sampling (LHS) is a well established procedure for defining pseudo-random designs of samples in  $\mathbb{R}^d$ , with good properties with respect to the uniform probability distribution on an hypercube  $[0, 1]^d$  (McKay et al., 1979; Owen, 1992a; Stein, 1987; Ranjan and Spencer, 2014; Ai et al., 2016). In particular, compared to a random sampling, a LHS: (i) enhances the capability to fill the d-dimensional

space with a finite number of points, (ii) in case  $d > 1$ , avoids the overlapping of point locations in the one dimensional projections, (iii) reduces the dependence of the number of points necessary on the dimensionality  $d$ .

**Definition 1 (Latin hypercube sampling)** Let  $\Xi = \{\xi_i : i = 1, \dots, N\}$  be a set of points inside the  $d$ -dimensional hypercube  $C = [0, 1]^d$ . Let  $[0, 1] = \bigcup_{j=1}^N I_j$ , where  $I_j = [\frac{(j-1)}{N}, \frac{j}{N}]$ . Let  $\xi_i = (\xi_i^1, \dots, \xi_i^d)$ , and for each  $k \in \{1, \dots, d\}$ , let  $\Xi^k = \{\xi_i^k : i = 1, \dots, N\}$ . Let  $\lambda^d$  be the uniform probability measure supported inside  $C$ , called Lebesgue measure. Then  $\Xi$  is a latin hypercube w.r.t.  $\lambda^d \iff \forall j \in \{1, \dots, N\}, \forall k \in \{1, \dots, d\}, |I_j \cap \Xi^k| = 1$ .

The procedure is simple: once the desired number of samples  $N \in \mathbb{N}$  is selected, and  $[0, 1]$  is divided in  $N$  equal bins, then each bin will contain one and only one projection of the samples over every coordinate. The LHS definition is trivially generalized over  $C = \prod_i^d [a_i, b_i]$ , i.e. the cartesian product of  $d$  arbitrary intervals. That will be applied in this study, defining LHS over the parameter domain of the flow models.

There are a large number of possible designs, corresponding the number of permutations of the bins in the  $d$ -projections, i.e.  $d \cdot N!$ . If the permutations are randomly sampled there is a high possibility that the design will have good properties. However, this is not assured, and clusters of points or regions of void space may be observed in  $C$ . For this reason, we base our design on the orthogonal arrays (OA) (Owen, 1992b; Tang, 1993).

**Definition 2 (Orthogonal arrays)** Let  $S = \{1, \dots, s\}$ , where  $s \geq 2$ . Let  $Q \in S^{n \times m}$  be a matrix of such integer values. Then  $Q$  is called an  $OA(n, m, s, r) \iff$  each  $n \times r$  submatrix of  $Q$  contains all possible  $1 \times r$  row vectors with the same frequency  $\lambda = n/s^r$ , which is called the index of the array. In particular,  $r$  is called the strength,  $n$  the size, ( $m \geq r$ ) the constrains, and  $s$  the levels of the array.

Orthogonal arrays are very useful for defining latin hypercubes which are also forced to fill the space (or its  $r$ -dimensional subspaces) in a more robust way, at the cost of potentially requiring a larger number of points than a traditional LHS.

**Proposition 3** Let  $Q$  be an  $OA(n, m, s, r)$ . Then let  $U \in \mathbb{R}^{n \times m}$  be defined as follows:

$$\forall k \in \{1, \dots, s\}, \forall j \in \{1, \dots, m\}, \{Q[\cdot, j] : Q[i, j] = k\} = \Pi((k-1)\lambda s^{r-1}, \dots, k\lambda s^{r-1}),$$

where  $\Pi$  is a random permutation of  $\lambda s^{r-1}$  elements. Then  $\Xi = \{\xi_i = U[i, \cdot] : i = 1, \dots, n\}$  is a LHS w.r.t to  $\lambda^m$  over  $C = [0, 1]^m$ . Moreover, let  $[0, 1]^r = \bigcup_{(h_1, \dots, h_r)=1}^s I_{(h_i)}$ , where  $I_{(h_i)} = \prod_i^r [\frac{(h_i-1)}{s}, \frac{h_i}{s}]$ . Then  $\forall D = (d_1, \dots, d_r) \subseteq \{1, \dots, m\}$ , let  $\Xi^D = \{(\xi^{d_1}, \dots, \xi^{d_r}) : i = 1, \dots, n\}$ . We have that

$$\forall k \in \{1, \dots, s\}, \forall (h_i : i = 1, \dots, r) \in \{1, \dots, d\}^r, |I_{(h_i)} \cap \Xi^D| = \lambda.$$

For each column of  $Q$  we are replacing the  $\lambda s^{r-1}$  elements with entry  $k$  by a random permutation of  $((k-1)\lambda s^{r-1} + h)_{h \in \{1, \dots, \lambda s^{r-1}\}}$ . After the replacement procedure is done, the newly obtained matrix  $U$  is equivalent to a LHS which inherits from  $Q$  the property of fully covering  $s^r$  equal  $r$ -dimensional hypercubes in every  $r$ -dimensional projection. Each hypercube contains  $\lambda$  points. In other words, inside each  $r$ -dimensional projection, the design associated to  $U$  fills the space like a regular grid at the scale of those  $s^r$  hypercubes, but it is still an LHS at a finer scale, i.e. the  $\lambda s^{r-1}$  one dimensional bins. A complete proof can be found in Tang (1993) and it is a straightforward verification of the required properties.

However, even in an LHS based on an  $OA(n, m, s, r)$ , if  $r < m$  what happens in the projections with dimension  $r' > r$  is not controlled, and randomizing procedures are made more difficult by the additional structure imposed by the OA. Moreover, the total number of points necessary to achieve a full design increases with  $r$ , and hence is affected by dimensionality issues.

Dealing with relatively small  $d$ , i.e.  $d \in \{3, 4\}$ , we adopt a LHS  $U$  created by a  $OA(s^d, d, s, d)$ . The strength is equal to the dimension  $d$ , hence the design fills the entire space like a  $d$  dimensional grid, but it is a LHS as well. In this case there is one point in each hypercube, and  $\lambda = 1$ . We take  $s = 8$  for the 3-dimensional designs over the parameter space of Mohr-Coulomb and Voellmy-Salm models, i.e. 512 points; we took  $s = 6$  for the 4-dimensional designs over the more complex parameter space of the Pouliquen-Forterre model, i.e. 1296 points.

## 9 Appendix B: Force contribution coefficients, and their conditional decomposition

The *contribution coefficients* are normalized quantities related to the force terms. They are obtained dividing the force terms described in section 3.2 by a dominant function  $\Phi$ . This is a tool to compare the different force terms, scaling the plots by the dominant function  $\Phi$  - in this case in  $[-1, 1]$ . It also represent the degree of relevance of the assumptions behind the force terms, changing as a function of time.

In general we focus on the moduli of the forces, or their projection on the slope direction. Hence, in the following the forces are scalar and not vectorial terms. It is important to remark that all the forces depend on the input variables, and they are thus considered as random variables. The definitions are not depending on the location, but all the results will significantly depend of that choice. Next notation will assume to be in a selected location  $x = L_k$ , where  $k \geq 1$ .

**Definition 4 (Contribution coefficients)** Let  $(F_i)_{i \in I}$  be random variables on  $(\Omega, \mathcal{F}, P)$ , representing the considered force components in location  $x$  at time  $t$ . Then, for each component  $i$ , the contribution coefficient is defined as:

$$C_i := \mathbb{E} \left[ \frac{F_i}{\Phi} \right],$$

where  $\Phi$  is a dominating function, i.e.  $\Phi \geq |F_i|, \forall i \in I$ .

The *total force*, i.e  $\sum_i F_i$  excluding the inertial terms, is not a good candidate for a dominating function. Indeed, the terms often have opposite signs, and their sum can be really small. Another issue is given by the existence of a subset of times  $\Theta$  characterized by the absence of flow in the selected location  $x$ . In  $\Theta$  the dominant force is null, and cannot be the denominator of a fraction.

We have tested two alternative  $\Phi$  choices:  $\Phi_1$  is based on the  $l^1$  norm, and defined as:

$$\Phi_1 := \begin{cases} \sum_i \frac{|F_i|}{2}, & \text{if not null;} \\ 1, & \text{otherwise.} \end{cases}$$

In contrast  $\Phi_2$  is a dominant force based on the  $l^\infty$  norm:

$$\Phi_2 := \begin{cases} \max_i |F_i|, & \text{if not null;} \\ 1, & \text{otherwise.} \end{cases}$$

In particular, for a particular location  $x$ , time  $t$ , and parameter sample  $\omega$ , we have  $C_i = 0$  if there is no flow or all the forces are null. The expectation of  $C_i$  is reduced by the chance of  $F_i$  being small compared to the other terms, or by the chance of having no flow in  $(x, t)$ . Moreover,  $\mathbb{E}[C_i] \in [-1, 1], \forall i$ .

**Proposition 5** Let  $\Phi_k, k = 1, 2$  be the functions described above. Then they are well defined dominating function, i.e.  $\Phi_k \geq |F_j|, \forall j, k$ .

**Proof.** If  $k = 1$ , the Newton equation states  $\sum_{j \in J} F_j = \sum_{i \in I} F_i$ , where  $(F_j)_{j \in J}$  are inertial forces, and  $(F_i)_{i \in I}$  the local forces. Then,  $\forall h \in I$

$$F_h = \sum_{i \neq h, i \in I} F_i - \sum_{j \in J} F_j.$$

And hence

$$|F_h| \leq |F_h| + \sum_{i \neq h, i \in I} |F_i| - \sum_{j \in J} |F_j| = 2\Phi_1.$$

A similar equation is valid  $\forall k \in J$ . If  $k = 2$ , or if the inertial forces are not included, the proof is trivial.

□

Furthermore, assuming  $\Phi = \Phi_2$ , there is a useful result explaining the meaning of those coefficients through the conditional expectation.

**Proposition 6** Let  $(F_i)_{i \in I}$  be random variables on  $(\Omega, \mathcal{F}, P)$ , representing the considered force components in location  $x$  at time  $t$ . For each  $i$ , let  $C_i$  be the contribution coefficient of force  $F_i$ , assuming  $\Phi = \Phi_2$ . Then we have the following expression:

$$C_i = \sum_j p_j \mathbb{E} \left[ \frac{F_i}{|F_j|} \mid \Phi = |F_j| \right],$$

where  $p_j := P\{\Phi = |F_j|\}$ .

**Proof.** Let  $Z$  be a discrete random variable such that, for each  $j \in \mathbb{N}$ ,  $(Z = j) \iff (\Phi = |F_j|)$ . Then, by the rule of chain expectation:

$$\begin{aligned} C_i &= \mathbb{E}\left[\frac{F_i}{\Phi}\right] = \mathbb{E}\left[\mathbb{E}\left[\frac{F_i}{\Phi} \mid Z = j\right]\right] = \\ &= \mathbb{E}\left[\mathbb{E}\left[\frac{F_i}{|F_j|} \mid Z = j\right]\right] = \sum_j P\{Z = j\} \mathbb{E}\left[\frac{F_i}{|F_j|} \mid Z = j\right]. \end{aligned}$$

Moreover, by definition,  $p_j = P\{Z = j\}$ . This completes the proof.  $\square$

The last proposition brings to a conditional decomposition of the contribution coefficients, taking advantage of the *dominance factors*  $(p_j)_{j=1,\dots,k}$ , i.e. the probability of each  $F_j$  to be the dominant force in  $(x, t)$ .

**Definition 7 (Conditional contributions and dominance factors)** *Let  $(F_i)_{i=1,\dots,k}$  be random variables on  $(\Omega, \mathcal{F}, P)$ , representing arbitrary force components in location  $x$  at time  $t$ . Then, for each pair of components  $(i, j)$ , the conditional contribution  $C_{i,j}$  is defined as:*

$$C_{i,j} := \mathbb{E}\left[\frac{F_i}{|F_j|} \mid \Phi = |F_j|\right],$$

where  $\Phi = \Phi_2$  is the dominant force. In particular, for each component  $i$ , the dominance factor is defined as:

$$p_j := P\{\Phi = |F_j|\}.$$

Example of the Contribution Coefficients in the cases studies of this paper are reported in the Supporting Information S6 and S7. They represent an additional tool to compare the different force terms, following a less restrictive approach than the Dominance Factors.

## References

- Aghakhani, H., Dalbey, K., Salac, D., and Patra, A. K. (2016). Heuristic and Eulerian interface capturing approaches for shallow water type flow and application to granular flows. *Computer Methods in Applied Mechanics and Engineering*, 304:243–264.
- Ai, M., Kong, X., and Li, K. (2016). A general theory for orthogonal array based latin hypercube sampling. *Statistica Sinica*, (26):761–777.
- Balmforth, N. J. and Kerswell, R. R. (2005). Granular collapse in two dimensions. *Journal of Fluid Mechanics*, 538:399–428.
- Barker, T., Schaeffer, D. G., Bohorquez, P., and Gray, J. M. N. T. (2015). Well-posed and ill-posed behaviour of the  $\mu(i)$ -rheology for granular flow. *Journal of Fluid Mechanics*, 779:794–818.
- Bartelt, P. and McArdell, B. (2009). Granulometric investigations of snow avalanches. *Journal of Glaciology*, 55(193):829–833(5).
- Bartelt, P., Salm, B., and Gruber, U. (1999). Calculating dense-snow avalanche runout using a voellmy-fluid model with active/passive longitudinal straining. *Journal of Glaciology*, 45(150):242–254.
- Batchelor, G. (2000). *An Introduction to Fluid Dynamics*. Cambridge Mathematical Libraries. Cambridge University Press.
- Bayarri, M. J., Berger, J. O., Calder, E. S., Dalbey, K., Lunagomez, S., Patra, A. K., Pitman, E. B., Spiller, E. T., and Wolpert, R. L. (2009). Using Statistical and Computer Models to Quantify Volcanic Hazards. *Technometrics*, 51(4):402–413.
- Bayarri, M. J., Berger, J. O., Calder, E. S., Patra, A. K., Pitman, E. B., Spiller, E. T., and Wolpert, R. L. (2015). Probabilistic Quantification of Hazards: A Methodology Using Small Ensembles of Physics-Based Simulations and Statistical Surrogates. *International Journal for Uncertainty Quantification*, 5(4):297–325.
- Bursik, M., Patra, A., Pitman, E., Nichita, C., Macias, J., Saucedo, R., and Girina, O. (2005). Advances in studies of dense volcanic granular flows. *Reports on Progress in Physics*, 68(2):271.
- Capra, L., Gavilanes-Ruiz, J. C., Bonasia, R., Saucedo-Giron, R., and Sulpizio, R. (2015). Re-assessing volcanic hazard zonation of volcán de colima, méxico. *Natural Hazards*, 76(1):41–61.
- Capra, L., Macís, J., Cortés, A., Dávila, N., Saucedo, R., Osorio-Ocampo, S., Arce, J., Gavilanes-Ruiz, J., Corona-Chávez, P., García-Sánchez, L., Sosa-Ceballos, G., and Vázquez, R. (2016). Preliminary report on the july 10–11, 2015 eruption at volcán de colima: Pyroclastic density currents with exceptional runouts and volume. *Journal of Volcanology and Geothermal Research*, 310(Supplement C):39 – 49.
- Capra, L., Manea, V. C., Manea, M., and Norini, G. (2011). The importance of digital elevation model resolution on granular flow simulations: a test case for colima volcano using titan2d computational routine. *Natural Hazards*, 59(2):665–680.
- Charbonnier, S., Germa, A., Connor, C., Gertisser, R., Preece, K., Komorowski, J.-C., Lavigne, F., Dixon, T., and Connor, L. (2013). Evaluation of the impact of the 2010 pyroclastic density currents at merapi volcano from high-resolution satellite imagery, field investigations and numerical simulations. *Journal of Volcanology and Geothermal Research*, 261(Supplement C):295 – 315. Merapi eruption.
- Charbonnier, S. J. and Gertisser, R. (2009). Numerical simulations of block-and-ash flows using the titan2d flow model: examples from the 2006 eruption of merapi volcano, java, indonesia. *Bulletin of Volcanology*, 71(8):953–959.
- Christen, M., Kowalski, J., and Bartelt, P. (2010). RAMMS: Numerical simulation of dense snow avalanches in three-dimensional terrain. *Cold Regions Science and Technology*, 63:1–14.
- DaCruz, F., Emam, S., Prochnow, M., Roux, J.-N., and Chevoir, F. (2005). Rheophysics of dense granular materials: Discrete simulation of plane shear flows. *Physical Review E*, 72:021309.

- Dade, W. B. and Huppert, H. E. (1998). Long-runout rockfalls. *Geology*, 26(9):803–806.
- Dalbey, K., Patra, A. K., Pitman, E. B., Bursik, M. I., and Sheridan, M. F. (2008). Input uncertainty propagation methods and hazard mapping of geophysical mass flows. *Journal of Geophysical Research: Solid Earth*, 113:1–16.
- Dalbey, K. R. (2009). *Predictive Simulation and Model Based Hazard Maps*. PhD thesis, University at Buffalo.
- Davila, N., Capra, L., Gavilanes-Ruiz, J., Varley, N., Norini, G., and Vazquez, A. G. (2007). Recent lahars at volcán de colima (mexico): Drainage variation and spectral classification. *Journal of Volcanology and Geothermal Research*, 165(3):127 – 141.
- Denlinger, R. P. and Iverson, R. M. (2001). Flow of variably fluidized granular masses across three-dimensional terrain: 2. Numerical predictions and experimental tests. *Journal of Geophysical Research*, 106(B1):553–566.
- Denlinger, R. P. and Iverson, R. M. (2004). Granular avalanches across irregular three-dimensional terrain: 1. Theory and computation. *Journal of Geophysical Research (Earth Surface)*, 109(F1):F01014.
- Edwards, A. N. and Gray, J. M. N. T. (2015). Erosion-deposition waves in shallow granular free-surface flows. *Journal of Fluid Mechanics*, 762:35–67.
- Fischer, J., Kowalski, J., and Pudasaini, S. P. (2012). Topographic curvature effects in applied avalanche modeling. *Cold Regions Science and Technology*, 74–75:21–30.
- Forterre, Y. (2006). Kapiza waves as a test for three-dimensional granular flow rheology. *Journal of Fluid Mechanics*, (563):123–132.
- Forterre, Y. and Pouliquen, O. (2002). Stability analysis of rapid granular chute flows: formation of longitudinal vortices. *Journal of Fluid Mechanics*, 467:361–387.
- Forterre, Y. and Pouliquen, O. (2003). Long-surface-wave instability in dense granular flows. *Journal of Fluid Mechanics*, 486:21–50.
- Forterre, Y. and Pouliquen, O. (2008). Flows of dense granular media. *Annual Review of Fluid Mechanics*, 40(1):1–24.
- Fraccarollo, L. and Toro, E. F. (1995). Experimental and numerical assessment of the shallow water model for two dimensional dam-break type problems. *Journal of Hydraulic Research*, 33:843–864.
- Freundt, A. and Bursik, M. I. (1998). Pyroclastic flow transport mechanisms. In Freundt, A. and Rosi, M., editors, *From Magma to Tephra: Modelling Physical Processes of Explosive Volcanism*, volume 4 of *Advances in Volcanology*, pages 151–222. Elsevier Science, Amsterdam.
- González, M. B., Ramírez, J. J., and Navarro, C. (2002). Summary of the historical eruptive activity of volcán de colima, mexico 1519–2000. *Journal of Volcanology and Geothermal Research*, 117(1):21 – 46.
- Gray, J. M. N. T. and Edwards, A. N. (2014). A depth-averaged  $\mu(I)$ -rheology for shallow granular free-surface flows. *Journal of Fluid Mechanics*, 755:503–534.
- Gray, J. M. N. T., Tai, Y. C., and Noelle, S. (2003). Shock waves, dead zones and particle-free regions in rapid granular free-surface flows. *Journal of Fluid Mechanics*, 491:161–181.
- Gray, J. M. N. T., Wieland, M., and Hutter, K. (1999). Gravity-driven free surface flow of granular avalanches over complex basal topography. *Proceedings of the Royal Society A: Mathematical, Physical and Engineering Sciences*, 455(1985):1841–1874.
- Greve, R., Koch, T., and Hutter, K. (1994). Unconfined flow of granular avalanches along a partly curved surface: experiments and theoretical predictions. *Proc. R. Soc. London Ser. A*, 342:573–600.

- Gruber, U. and Bartelt, P. (2007). Snow avalanche hazard modelling of large areas using shallow water numerical models and GIS. *Environmrntal Modelling & Software*, 22:1472–1481.
- Hokanardottir, K. M. and Hogg, A. J. (2005). Oblique shocks in rapid granular flows. *Phys. Fluids*, 17:077101.
- Hutter, K., Siegel, M., Savage, S. B., and Nohguchi, Y. (1993). Two-dimensional spreading of a granular avalanche down an inclined plane part I. Theory. *Acta Mechanica*, 100:37–68.
- Hyman, D. and Bursik, M. (2018). Time-Dependence of Passive Degassing at Volcán Popocatépetl, Mexico from Infrared Measurements: Implications for Gas Pressure Distribution and Lava Dome Stability. *Journal of Geophysical Research*, (in preparation).
- Iordanoff, I. P. and Khonsari, M. M. (2004). Granular Lubrication: Toward an Understanding of the Transition Between Kinetic and Quasi-Fluid Regime. *Journal of Tribology*, 126(1):137–145.
- Iverson, R. M. (1997). The physics of debris flows. *Reviews of Geophysics*, 35:245–296.
- Iverson, R. M. and Denlinger, R. P. (2001). Flow of variably fluidized granular masses across three-dimensional terrain: 1. Coulomb mixture theory. *Journal of Geophysical Research*, 106(B1):537.
- Iverson, R. M. and George, D. L. (2014). A depth-averaged debris-flow model that includes the effects of evolving dilatancy. i. physical basis. *Proceedings of the Royal Society of London A: Mathematical, Physical and Engineering Sciences*, 470(2170).
- Iverson, R. M., Logan, M., and Denlinger, R. P. (2004). Granular avalanches across irregular three-dimensional terrain: 2. experimental tests. *Journal of Geophysical Research: Earth Surface*, 109(F1):n/a–n/a. F01015.
- Jaeger, H. M., Liu, C., and Nagel, S. R. (1989). Relaxation at the Angle of Repose. *Physical Review Letters*, 62(1):40–43.
- Jop, P., Forterre, Y., and Pouliquen, O. (2006). A constitutive law for dense granular flows. *Nature*, 441:727–730.
- Kelfoun, K. (2011). Suitability of simple rheological laws for the numerical simulation of dense pyroclastic flows and long-runout volcanic avalanches. *Journal of Geophysical Research*, 116:B08209.
- Kelfoun, K. and Druitt, T. H. (2005). Numerical modeling of the emplacement of socompa rock avalanche, chile. *Journal of Geophysical Research: Solid Earth*, 110(B12).
- Kelfoun, K., Samaniego, P., Palacios, P., and Barba, D. (2009). Testing the suitability of frictional behaviour for pyroclastic flow simulation by comparison with a well-constrained eruption at Tungurahua volcano (Ecuador). *Bulletin of Volcanology*, 71:1057–1075.
- Kern, M., Bartelt, P., Sovilla, B., and Buser, O. (2009). Measured shear rates in large dry and wet snow avalanches. *Journal of Glaciology*, 55(190):327–338.
- la Cruz-Reyna, S. D. (1993). Random patterns of occurrence of explosive eruptions at colima volcano, mexico. *Journal of Volcanology and Geothermal Research*, 55(1):51 – 68.
- Lajeunesse, E., Monnier, J. B., and Homsy, G. M. (2005). Granular slumping on a horizontal surface. *Phys. Fluids*, 17:103302.
- Luca, I., Tai, Y., and Kuo, C. (2016). *Shallow Geophysical Mass Flows down Arbitrary Topography: Model Equations in Topography-fitted Coordinates, Numerical Simulation and Back-calculations of Disastrous Events*. Advances in Geophysical and Environmental Mechanics and Mathematics. Springer International Publishing.
- Macorps, E., Charbonnier, S. J., Varley, N. R., Capra, L., Atlas, Z., and Cabré, J. (2018). Stratigraphy, sedimentology and inferred flow dynamics from the july 2015 block-and-ash flow deposits at volcán de colima, mexico. *Journal of Volcanology and Geothermal Research*, 349:99 – 116.

- Mangeney-Castelnau, A., Bouchut, F., Thomas, N., Vilotte, J. P., and Bristeau, M.-O. (2007). Numerical modeling of self-channeling granular flows and of their levee/channel deposits. *J. Geophys. Res.*, 112:F02017.
- Mangeney-Castelnau, A., Bouchut, F., Vilotte, J. P., Lajeunesse, E., Aubertin, A., and Pirulli, M. (2005). On the use of Saint-Venant equations to simulate the spreading of a granular mass. *J. Geophys. Res.*, 110:B09103.
- Martin Del Pozzo, A. M., Sheridan, M. F., Barrera, M., Hubp, J. L., and Selem, L. V. (1995). Potential hazards from Colima Volcano, Mexico. *Geofisica Internacional*, 34:363–376.
- McKay, M. D., Beckman, R. J., and Conover, W. J. (1979). A comparison of three methods for selecting values of input variables in the analysis of output from a computer code. *Technometrics*, 21(2):239–245.
- Norini, G., De Beni, E., Andronico, D., Polacci, M., Burton, M., and Zucca, F. (2009). The 16 november 2006 flank collapse of the south-east crater at mount etna, italy: Study of the deposit and hazard assessment. *Journal of Geophysical Research: Solid Earth*, 114(B2):n/a–n/a. B02204.
- Ogburn, S. E., Berger, J., Calder, E. S., Lopes, D., Patra, A., Pitman, E. B., Rutarindwa, R., Spiller, E., and Wolpert, R. L. (2016). Pooling strength amongst limited datasets using hierarchical bayesian analysis, with application to pyroclastic density current mobility metrics. *Statistics in Volcanology*, 2:1–26.
- Owen, A. B. (1992a). A Central Limit Theorem for Latin Hypercube Sampling. *Journal of the Royal Statistical Society*, 54(2):541–551.
- Owen, A. B. (1992b). Orthogonal arrays for computer experiments, integration and visualization. *Statistica Sinica*, 2(2):439–452.
- Patra, A., Nichita, C., Bauer, A., Pitman, E., Bursik, M., and Sheridan, M. (2006). Parallel adaptive discontinuous galerkin approximation for thin layer avalanche modeling. *Computers & Geosciences*, 32(7):912 – 926. Computer Simulation of natural phenomena for Hazard Assessment.
- Patra, A. K., Bauer, A. C., Nichita, C. C., Pitman, E. B., Sheridan, M. F., Bursik, M., Rupp, B., Webber, A., Stinton, A. J., Namikawa, L. M., and Renschler, C. S. (2005). Parallel adaptive numerical simulation of dry avalanches over natural terrain. *Journal of Volcanology and Geothermal Research*, 139(1-2):1–21.
- Pirulli, M., Bristeau, M. O., Mangeney, A., and Scavia, C. (2007). The effect of the earth pressure coefficients on the runout of granular material. *Environmental Modelling & Software*, 22(10):1437–1454.
- Pirulli, M. and Mangeney, A. (2008). Results of Back–Analysis of the Propagation of Rock Avalanches as a Function of the Assumed Rheology. *Rock Mechanics and Rock Engineering*, 41(1):59–84.
- Pitman, E., Nichita, C., Patra, A., Bauer, A., Bursik, M., and Webb, A. (2003a). A model of granular flows over an erodible surface. *Discrete and Continuous Dynamical Systems - Series B*, 3(4):589–599.
- Pitman, E. B. and Le, L. (2005). A two-fluid model for avalanche and debris flows. *Philosophical transactions. Series A, Mathematical, physical, and engineering sciences*, 363(1832):1573–601.
- Pitman, E. B., Nichita, C. C., Patra, A., Bauer, A., Sheridan, M., and Bursik, M. (2003b). Computing granular avalanches and landslides. *Physics of Fluids*, 15(12):3638.
- Pouliquen, O. (1999). Scaling laws in granular flows down rough inclined planes. *Physics of Fluids*, 11(3):542–548.
- Pouliquen, O. and Forterre, Y. (2002). Friction law for dense granular flows: application to the motion of a mass down a rough inclined plane. *Journal of Fluid Mechanics*, 453:133–151.

- Procter, J. N., Cronin, S. J., Platz, T., Patra, A., Dalbey, K., Sheridan, M., and Neall, V. (2010). Mapping block-and-ash flow hazards based on titan 2d simulations: a case study from mt. taranaki, nz. *Natural Hazards*, 53(3):483–501.
- Pudasaini, S. and Hutter, K. (2007). *Avalanche Dynamics: Dynamics of Rapid Flows of Dense Granular Avalanches*. Springer.
- Pudasaini, S. P. and Hutter, K. (2003). Rapid shear flows of dry granular masses down curved and twisted channels. *Journal of Fluid Mechanics*, 495:193–208.
- Ranjan, P. and Spencer, N. (2014). Space-filling latin hypercube designs based on randomization restrictions in factorial experiments. *Statistics and Probability Letters*, 94(Supplement C):239 – 247.
- Rankine, W. J. M. (1857). On the Stability of Loose Earth. *Phil. Trans. R. Soc. Lond.*, 147(2):9–27.
- Reyes-Dávila, G. A., Arámbula-Mendoza, R., Espinasa-Perena, R., Pankhurst, M. J., Navarro-Ochoa, C., Savov, I., Vargas-Bracamontes, D. M., Cortés-Cortés, A., Gutiérrez-Martínez, C., Valdés-González, C., Domínguez-Reyes, T., González-Amezcua, M., Martínez-Fierros, A., Ramírez-Vázquez, C. A., Cárdenas-González, L., Castaneda-Bastida, E., de los Monteros, D. M. V. E., Nieto-Torres, A., Champion, R., Courtois, L., and Lee, P. D. (2016). Volcan de colima dome collapse of july, 2015 and associated pyroclastic density currents. *Journal of Volcanology and Geothermal Research*, 320(Supplement C):100 – 106.
- Rupp, B. (2004). An analysis of granular flows over natural terrain. Master's thesis, University at Buffalo.
- Rupp, B., Bursik, M., Namikawa, L., Webb, A., Patra, A. K., Saucedo, R., Macías, J. L., and Renschler, C. (2006). Computational modeling of the 1991 block and ash flows at Colima Volcano, México. *Geological Society of America Special Papers*, 402(11):223–237.
- Ruyer-Quil, C. and Manneville, P. (2000). Improved modeling of flows down inclined planes. *Eur. Phys. J. B*, 15:357–369.
- Salm, B. (1993). Flow, flow transition and runout distances of flowing avalanches. *Annals of Glaciology*, 18:221–226.
- Salm, B., Burkard, A., and Gubler, H. (1990). Berechnung von Fliesslawinen: eine Anleitung für Praktiker mit Beispielen. *Mitteilungen des Eidgenössische Institutes für Schnee- und Lawinenforschung*, 47.
- Sarocchi, D., Sulpizio, R., Macías, J., and Saucedo, R. (2011). The 17 july 1999 block-and-ash flow (baf) at colima volcano: New insights on volcanic granular flows from textural analysis. *Journal of Volcanology and Geothermal Research*, 204(1):40 – 56.
- Saucedo, R., Macías, J., Bursik, M., Mora, J., Gavilanes, J., and Cortes, A. (2002). Emplacement of pyroclastic flows during the 1998–1999 eruption of volcán de colima, méxico. *Journal of Volcanology and Geothermal Research*, 117(1):129 – 153.
- Saucedo, R., Macías, J., Gavilanes, J., Arce, J., Komorowski, J., Gardner, J., and Valdez-Moreno, G. (2010). Eyewitness, stratigraphy, chemistry, and eruptive dynamics of the 1913 plinian eruption of volcán de colima, méxico. *Journal of Volcanology and Geothermal Research*, 191(3–4):149 – 166.
- Saucedo, R., Macías, J., Sheridan, M., Bursik, M., and Komorowski, J. (2005). Modeling of pyroclastic flows of colima volcano, mexico: implications for hazard assessment. *Journal of Volcanology and Geothermal Research*, 139(1):103 – 115. Modeling and Simulation of Geophysical Mass Flows.
- Saucedo, R., Macías, J. L., and Bursik, M. (2004). Pyroclastic flow deposits of the 1991 eruption of Volcán de Colima, Mexico. *Bulletin of Volcanology*, 66(4):291–306.
- Savage, S. B. and Hutter, K. (1989). The motion of a finite mass of granular material down a rough incline. *Journal of Fluid Mechanics*, 199:177.

- Savage, S. B. and Iverson, R. M. (2003). Surge dynamics coupled to pore-pressure evolution in debris flows. *Debris-Flow Hazards Mitigation: Mechanics, Prediction and Assessment*, edited by: Rickenmann, D. and Chen, C. L., Millpress, 1:503–514.
- Sheridan, M., Stinton, A., Patra, A., Pitman, E., Bauer, A., and Nichita, C. (2005). Evaluating titan2d mass-flow model using the 1963 little tahoma peak avalanches, mount rainier, washington. *Journal of Volcanology and Geothermal Research*, 139(1):89 – 102. Modeling and Simulation of Geophysical Mass Flows.
- Sheridan, M. F. and Macías, J. L. (1995). Estimation of risk probability for gravity-driven pyroclastic flows at volcan colima, mexico. *Journal of Volcanology and Geothermal Research*, 66(1):251 – 256. Models of Magnetic Processes and Volcanic Eruptions.
- Sheridan, M. F., Patra, A. K., Dalbey, K., and Hubbard, B. (2010). *Probabilistic digital hazard maps for avalanches and massive pyroclastic flows using TITAN2D.*, volume Stratigraphy and geology of volcanic areas, 464, chapter 14, page 281. Geological Society of America.
- Silbert, L. E., Ertas, D., Grest, G. S., Halsey, T. C., Levine, D., and Plimpton, S. J. (2001). Granular flow down an inclined plane: Bagnold scaling and rheology. *Physical Review E*, 64(5):051302.
- Spiller, E. T., Bayarri, M. J., Berger, J. O., Calder, E. S., Patra, A. K., Pitman, E. B., and Wolpert, R. L. (2014). Automating emulator construction for geophysical hazard maps. *SIAM/ASA Journal on Uncertainty Quantification*, 2(1):126–152.
- Stefanescu, E. R., Bursik, M., Cordoba, G., Dalbey, K., Jones, M. D., Patra, A. K., Pieri, D. C., Pitman, E. B., and Sheridan, M. F. (2012a). Digital elevation model uncertainty and hazard analysis using a geophysical flow model. *Proceedings of the Royal Society of London A: Mathematical, Physical and Engineering Sciences*, 468(2142):1543–1563.
- Stefanescu, E. R., Bursik, M., and Patra, A. K. (2012b). Effect of digital elevation model on mohr-coulomb geophysical flow model output. *Natural Hazards*, 62(2):635–656.
- Stein, M. (1987). Large sample properties of simulations using latin hypercube sampling. *Technometrics*, 29(2):143–151.
- Sulpizio, R., Capra, L., Sarocchi, D., Saucedo, R., Gavilanes-Ruiz, J., and Varley, N. (2010). Predicting the block-and-ash flow inundation areas at volcán de colima (colima, mexico) based on the present day (february 2010) status. *Journal of Volcanology and Geothermal Research*, 193(1):49 – 66.
- Tang, B. (1993). Orthogonal array-based latin hypercubes. *Journal of the American Statistical Association*, 88(424):1392–1397.
- Toro, E. (2013). *Riemann Solvers and Numerical Methods for Fluid Dynamics: A Practical Introduction*. Springer Berlin Heidelberg.
- Voellmy, A. (1955). Über die Zerstörungskraft von Lawinen. *Schweiz Bauzeitung*, 73:159–165, 212–217, 246–249, 280–285.
- Webb, A. (2004). Granular flow experiments to validate numerical flow model, TITAN2D. Master's thesis, University at Buffalo.
- Webb, A. and Bursik, M. (2016). Granular flow experiments for validation of numerical flow models. Technical report, University at Buffalo.
- Wieland, J. M., Gray, J. M. N. T., and Hutter, K. (1999). Channelized free-surface flow of cohesionless granular avalanches in a chute with shallow lateral curvature. *Journal of Fluid Mechanics*, 392:73–100.
- Wolpert, R. L., Ogburn, S. E., and Calder, E. S. (2016). The longevity of lava dome eruptions. *Journal of Geophysical Research: Solid Earth*, 121(2):676–686. 2015JB012435.

- Yu, B., Dalbey, K., Webb, A., Bursik, M., Patra, A. K., Pitman, E. B., and Nichita, C. (2009). Numerical issues in computing inundation areas over natural terrains using Savage-Hutter theory. *Natural Hazards*, 50(2):249–267.
- Zobin, V., Luhr, J., Taran, Y., Bretón, M., Cortés, A., Cruz-Reyna, S. D. L., Domínguez, T., Galindo, I., Gavilanes, J., Muniz, J., Navarro, C., Ramírez, J., Reyes, G., Ursúa, M., Velasco, J., Alatorre, E., and Santiago, H. (2002). Overview of the 1997–2000 activity of volcán de colima, méxico. *Journal of Volcanology and Geothermal Research*, 117(1):1 – 19.
- Zobin, V. M., Arámbula, R., Bretón, M., Reyes, G., Plascencia, I., Navarro, C., Téllez, A., Campos, A., González, M., León, Z., Martínez, A., and Ramírez, C. (2015). Dynamics of the january 2013–june 2014 explosive-effusive episode in the eruption of volcán de colima, méxico: insights from seismic and video monitoring. *Bulletin of Volcanology*, 77(4):31.